Beverage Deterioration Monitoring Based on Surface Tension Dynamics and Absorption Spectrum Analysis

Yongzhi Huang, Kaixin Chen, Jiayi Zhao, *Student Member, IEEE,* Lu Wang, *Senior Member, IEEE,* and Kaishun Wu, *Fellow, IEEE*

Abstract—Biochemical information sensing has always been one of the challenges in ubiquitous sensing research for mobile computing. Microorganisms will cause undetectable deterioration in drink production, such as wine and beverage, and microbial contamination is highly susceptible during storage like some liquors can be bottled for sometimes over ten years. Microbial culture methods are common for quality monitoring but unsuitable for real-time beverage quality monitoring. As far as we know, we are the first to use ubiquitous sensing for real-time microbial contamination detection. We designed a lightweight monitoring system called Microbe-Radar, which uses light signals to monitor real-time beverage quality. Microbe-Radar uses eight LEDs and a photodiode to detect fine-grained surface tension and absorption spectrum changes caused by microbial metabolites and growth during deterioration. Characteristic offset degree measurement and absorption spectrum dimension expansion are two critical technologies. Moreover, we implemented countermeasures against ambient light noise and sloshing interference. Microbe-Radar's surface tension and absorption spectrum measurement errors are only 0.89 mN/m and 2.4%, respectively, making identifying the contamination duration, microorganism content, and microorganism composition worthwhile. Experiments showed Microbe-Radar could determine potential issues with liquor quality when the liquid becomes health-threatening or even just contaminated, with an accuracy of 97.5%. Microbe-Radar can also be extended to beverage deterioration warning, with deterioration prediction accuracy of more than 90.6% for five beverages (milk, apple juice, etc.).

Index Terms—Liquid quality, Beverage deterioration, Long-term monitoring, Light signal, Absorption spectrum, Modeling, Fine-grained

1 Introduction

The ubiquitous sensing of mobile computing supports smart life. Existing research has extended perception to the changes in physical appearances, such as action recognition and positioning. Nonetheless, the precise detection of minute biochemical data has consistently been an area of obscurity in investigating pervasive sensing. The beverages manufacturing and the brewing and aging processing in wine production can mask food safety risks for months or even years. During this time, microorganisms grow and multiply [1]. The current techniques for measuring the quality of liquids, such as the spread plate method utilizing microbial cultures [2] and the detection of microbial presence through ATP fluorescence [3], are both laborious and costly.

Specialized wineries apply strict controls over their wine cellars' temperature and carbon dioxide concentration to reduce costs [1], [4]. These measures aim to create an environment conducive to the survival of yeasts. It is important to note that such controls are only effective in reducing the rate of pathogenic microorganism reproduction. Wine contamination is often undetectable until the end of the aging process and can have severe food safety implications in alcoholic beverages [5]. These substances that have undergone deterioration are perceived as a significant risk to food safety. They can cause various adverse effects on health, such as allergies, diarrhea, shock, and fever [6]–[8]. Late detection of deteriorating liquids has resulted in significant financial losses for manufacturers over an extended period. These liquids are teeming with pathogenic microorganisms [9], [10] like Vibrio casei, Staphylococcus aureus, Halomonas, Escherichia coli, Salmonella, Mucor, Penicillium, Aspergillus flavus, Aspergillus niger, and Serratia that produce toxic and dangerous substances [11], [12], such as ammonia, hydrogen sulfide, nitrite, and aflatoxin that can cause cancer. According to a 2020 report by the World Health Organization [13], approximately 600 million individuals, roughly one in every ten individuals globally, get sick from eating tainted food each year, with 420,000 fatalities leading to the loss of 33 million healthy life years (DALYs).

Safety testing in a winery involves two main sets of product tests: determining chemical indexes and microbial culture counts, including pH measurements [14], the spread plate method with microbial cultures [2], and microbial

- *Y. Huang is with the Hong Kong University Science and Technology (Guangzhou), Guangzhou 511458. E-mail: huangyongzhi@szu.edu.cn.*
- *K. Chen, J. Zhao, L. Wang are with the College of Computer Science and Software Engineering, Shenzhen University, Shenzhen 518060, P.R. China. E-mail: 2017133035, zhaojiayi2020@email.szu.edu.cn, wanglu@szu.edu.cn.*
- *K. Wu is with Hong Kong University of Science and Technology (Guangzhou), Guangzhou HKUST Fok Ying Tung Research Institute, Guangzhou 511458, and also with the College of Computer Science and Software Engineering, Shenzhen University, Shenzhen 518060, P.R. China, with the PCL Research Center of Networks and Communications, Peng Cheng Laboratory, Shenzhen, China. E-mail: wuks@ust.hk.*

(Corresponding author: Lu Wang.)

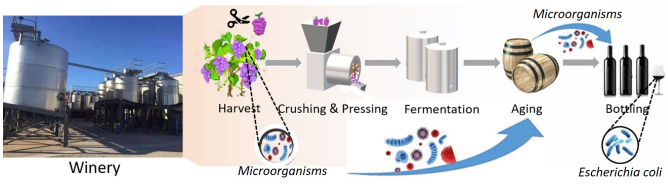

Fig. 1: Winery and brewing process.

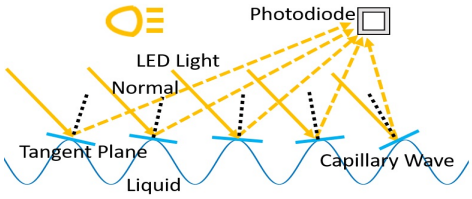

Fig. 2: Cross section schematic diagram.

detection based on ATP fluorescence [3], [15]. Such testing is time-consuming and cumbersome and has a high probability of inspection misses. Some researchers have designed an electronic nose [16] to identify deterioration through smell fingerprints. This expensive high-precision equipment can detect deterioration only when barrels are open and cannot detect real-time deterioration during production. The latest studies have used different technologies, including detection based on light signals [17]–[19], RFID [20], ultra-bandwidth signals [21], and mechanical vibrations [22], [23] to identify liquids, but they are difficult to employ in the production process.

In light of the aforementioned circumstances, we present inquiries aimed at addressing said predicaments. Is there an alternative to conventional methods of microbial cultivation? Can we attain real-time measurements of the quality of liquor utilizing commonplace instrumentation? Pertinent researchers have revealed that deterioration may affect liquid properties [18], [24], [25], especially at the surface. The surface tension of deteriorated liquids is altered [24], [25], and the microorganisms present within further modify the absorption spectrum subtly [18]. The microorganisms on a liquid surface change the composition by breaking down the initial nutrients and emitting metabolites. Thus, it is possible to monitor liquor quality in real time by performing measurements for surface tension and absorption spectrum in a time-effective manner.

Although numerous studies have proposed measurement methods for the surface tension [26]–[28] and absorption spectrum [29]–[31] of liquids, the acquisition of traditional detection instruments, which are large and expensive, is difficult for many laboratories. In the latest research, researchers have continued to increase the accessibility and simplicity of surface tension detection methods [32], [33]. For example, CapCam [33] uses a mobile phone's high-definition camera to measure the surface tension of a liquid through the bottom of a disposable paper cup. Still, it is challenging to measure nontransparent liquids, such as red wine, within a sealed container with this device.

This paper presents the Microbe-Radar system, a specialized technology designed for monitoring the quality of liquor using light signals. The lightweight system can be easily installed in brewing equipment after encapsulation. Unlike other expensive components like cameras, the system utilizes only 8 LEDs and a single photodiode, making it cost-efficient. The system activates a vibro-motor to generate capillary waves during measurement, and by analyzing the reflection of light, the system can detect subtle changes in surface tension caused by liquor deterioration. The system uses self-designed dimension expansion technology to adjust the LEDs to achieve fine-grain absorption spectrum measurements to identify small changes in liquor composition after vibration. This paper aims to convince experts in the field of brewing technology of the effectiveness and efficiency of the Microbe-Radar system.

Implementing this system poses several challenges that require careful consideration. Firstly, since a single photodiode cannot capture capillary waves directly through imaging, it is necessary to establish a suitable model for characterizing the wavelengths of these waves. Secondly, vibration disturbances can negatively affect the received light signal by producing multiple complex frequency signals, which can hinder our ability to identify the features associated with changes in capillary wave wavelengths. Furthermore, the narrow LED waveband means that reflected light can only display the absorption spectrum within this limited range. This compressed and coarse-grained information makes identifying subtle changes from microbial decomposition and metabolism tricky. Finally, reducing the effects of ambient interference poses a formidable challenge.

Contributions: As far as we know, we are the pioneers in introducing a novel and advanced liquor quality monitoring system called Microbe-Radar, which operates in real time. Microbe-Radar can be conveniently installed on brewing equipment to enable long-term monitoring of liquor quality. It is notable that Microbe-Radar consumes low power and is economically feasible for deployment on a large scale due to its usage of common instrumentation. Furthermore, we have devised a new surface tension measurement approach with a negligible error of only .89 mN/m. Lastly, we have also designed a dimension expansion technique for a coarse-grained absorption spectrum, enabling the detection of even the faintest changes in liquor components caused by decomposing the original nutrients and releasing metabolites.

The rest of the paper is organized as follows: Section 2 details how the LED and photodiode modules can detect the features of liquor surface tension and absorption spectra on the basis of theoretical models. Section 3 describes a feasibility study. After a system overview in Section 4, we introduce the system design and illustrate how we addressed the challenges in Section 5. Section 6 presents several case studies evaluating the system's performance. We discuss related work in Section 7 and conclusions and future work in Section 8.

2 THEORY OF OPERATIONS

This section will introduce the theoretical models for liquor quality detection.

2.1 Surface Tension

The property of liquids known as surface tension is of great significance. It is a well-known fact that the surface

molecules of any liquid try their best to decrease their contact area with air to conserve energy. This results in the creation of a force among them known as surface tension, which belongs to the class of van der Waals forces. Additionally, the expression can be used to relate surface tension to the angular frequency of a surface capillary wave, providing further credence to the importance of this property [34], [35]: $\varpi^2 = gK + \frac{\gamma K^3}{\rho}$. ϖ is the angular frequency of a surface capillary wave, K is the wavenumber of the surface capillary wave, γ is the surface tension, ρ is the liquid density, and g is acceleration due to gravity. Pathogenic microorganism contamination causes liquid quality deterioration and produces harmful carcinogenic metabolites. These microorganisms need oxygen to multiply and, therefore, first grow on the surface of a liquid. The decomposed nutrients and released metabolites from growing microorganisms affect the van der Waals forces between molecules, consequently changing the surface tension. By analyzing these changes, we can monitor liquor quality.

2.2 Principle behind the Surface Tension Measurement

We utilize the most commonly available light-emitting diodes (LEDs) and photodiodes regarding expense and energy usage. This section aims to explain how the application of LEDs and photodiodes can be utilized to measure the surface tension of the liquid. Since capillary waves are minute and distant from the LEDs, it's plausible to assume that the rays projected onto the liquid surface are parallel. According to Figure 2, due to the arc shape, each individual convex wave can only exist in a single tangent plane in compliance with the rule of reflection, which states that the angle of incidence is equal to the angle of reflection.

To find the reflection point locations, we model the reflective liquid. As shown in Figure 3, we assume that a surface capillary wave generated by a liquid is a sine curve, $y = \sin x$, and the point $(a_0, \sin a_0)$ on the curve is the reflection point. The receiver is a photodiode, located at the Cartesian axes (L, H). Then, we can obtain the tangent equation at this point as $y = \sin a_0 + \cos a_0 \, (x - a_0)$. Next, we can get the reflection path equation: $y = \frac{\sin a_0 - H}{a_0 - L} x - \frac{(\sin a_0 - H)L}{a_0 - L} + H$. Because the normal line is perpendicular to the tangent plane, we can infer that the normal line equation is $y = \sin a_0 - \frac{1}{\cos a_0} (x - a_0)$. At this moment, we can use y to calculate the reflection angle between the reflected ray and the normal $\alpha_1 = \arctan \left| \frac{\frac{\sin a_0 - H}{a_0 - L} + \frac{1}{\cos a_0}}{1 - \frac{\sin a_0 - H}{a_0 - L} \frac{1}{\cos a_0}} \right|$. As the incident rays are parallel, we assume that the angle with the horizontal plane is β. Then, we can obtain the incident angle between the incident ray and the normal, $\alpha_2 = \arctan \left| \frac{\tan \beta + \frac{1}{\cos a_0}}{1 - \frac{\tan \beta}{\cos a_0}} \right|$. We simultaneously set α_1 and α_2, let $\alpha_1 = \alpha_2$, set $a_0 = k\lambda + c$, and then obtain all feasible solutions, which are the tangent plane positions of each convex wave. Among them, λ is the capillary wave wavelength, k is a nonnegative integer, $0 < c < \lambda$.

Next, we use the feasible solutions to establish a simulation model. As shown in Figure 4 (a), we set two different liquid surface tensions γ_1 and γ_2 ($\gamma_1 > \gamma_2$), and the wavelengths of the capillary waves are λ_1 and λ_2 ($\lambda_1 > \lambda_2$). Considering that there will be scattering in light propagation, we set the area around the reflection point as the photodiode's receiving range. When the vibration generates capillary waves, they spread from the center to the surroundings, and these ripples will spread outward at a constant velocity V. We assume that the area inside the rectangle is the photodiode's receiving area. After that, we calculate the total light intensity received by the photodiode and observe the change over time. As shown in Figure 4 (b), lower surface tension will result in a higher frequency of the reflected light signal.

2.3 Modeling Multipath Effects in Microbe-Radar

In addition to the ideal case of direct reflection in Section 2.2 (shown in **Path 1** of Figure 5), there is also a multipath effect in the vessel. Each convex wave has only one tangent plane satisfying the reflection law so that the light of the LED is directly reflected in the position of the photodiode. However, other tangent planes of the convex wave can also reflect the incident light and may be reflected in the photodiode through the brewing vessel wall, as shown in **Path 2** of Figure 5. The incident light may also be reflected on the lid through other tangent planes of the convex wave, then reflected on the capillary wave through the lid, and finally received by the photodiode through the reflection of the brewing vessel wall, as shown in **Path 3** of Figure 5. It can be seen that the signal received by the photodiode is the superposition of the direct reflection signal and the multipath reflection signal. The model of the signal received by the photodiode is established as follows:

$$RSS(t) = \sum_{i=1}^{N_{LED}} \left(RSS_{direct\ i}(t) + \sum_{j=1}^{N_{multi}(t)} RSS_{multi\ ij}(t) \right) \tag{1}$$

where $RSS_{direct\ i}(t)$ represents the direct reflection path of the tangent plane satisfying the reflection law on the convex wave of the $i-th$ LED at time t. $RSS_{multi\ ij}(t)$ represents the $j-th$ multipath of the $i-th$ LED at time t. N_{LED} indicates the number of LEDs. $N_{multi}(t)$ is the number of multipaths at time t. Each multipath will undergo different propagation attenuation and reflection attenuation, and the time to reach the photodiode will have different delays. Therefore, the impulse response of each multipath can be expressed as:

$$RSS_{multi\ j}(t) = \sigma_j(t) \cdot \rho_j(t) \cdot h(t - \tau_j(t)) \tag{2}$$

where $\sigma_j(t)$ represents the attenuation rate of the $j-th$ multipath at time t, $\rho_j(t)$ represents the reflectivity of the $j-th$ multipath at time t, $h(t)$ represents the transmission signal of the $j-th$ multipath at time t, and $\tau_j(t)$ represents the time delay of the $j-th$ multipath at time t. Substituting Equation (2) into Equation (1), the signal received by photodiode at time t can be rewritten as:

$$RSS(t) = \sum_{i=1}^{N_{LED}} RSS_{direct\ i}(t) + \sum_{i=1}^{N_{LED}} \sum_{j=1}^{N_{multi}(t)} \sigma_{ij}(t) \cdot \rho_{ij}(t) \cdot h\left(t - \tau_{ij}(t)\right) \tag{3}$$

where $\sigma_{ij}(t)$ represents the attenuation rate of the $j-th$ multipath of the $i-th$ LED at time t, $\rho_{ij}(t)$ represents

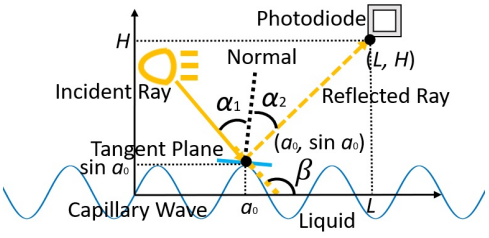

Fig. 3: Model of the location of a reflection point.

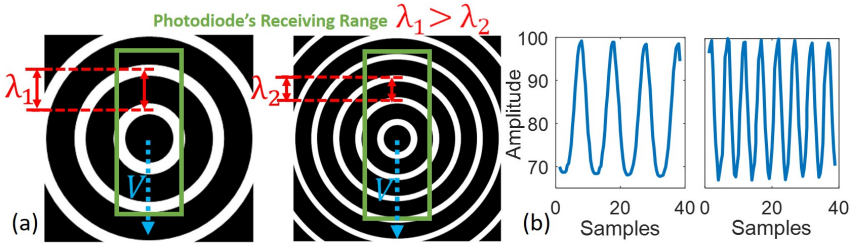

Fig. 4: Simulation model. (a) Top view. (b) Changes in the intensity of light received by the photodiode.

the reflectivity of the $j-th$ multipath of the $i-th$ LED at time t, $h(t)$ represents the transmission signal of the $j-th$ multipath of the $i-th$ LED at time t, and $\tau_{ij}(t)$ represents the time delay of the $j-th$ multipath of the $i-th$ LED at time t. Because the capillary wave generated by liquid vibration propagates continuously forward when t changes, the attenuation rate $\sigma_{ij}(t)$ and reflectivity $\rho_{ij}(t)$ of each multipath and time delay $\tau_{ij}(t)$ will change. Among these multipaths, some multipaths with few-times reflections may be regular, and it helps us to judge the propagation frequency of capillary wave (such as **Path 2** after two reflections in Figure 5). However, some multipaths are irregular. These paths may cause interference peaks in the signal spectrum and interfere with the identification of capillary wave propagation frequency (such as **Path 3** after five reflections in Figure 5). Suppose we collect $n-points$ signal, we write $RSS(t)$ as the formula $RSS(n)$ about n. Then we do the following Fast Fourier Transform (FFT) for $RSS(n)$:

$$RSS(k)=FFT\left[RSS(n)\right]=\sum_{n=0}^{N-1}\left(\sum_{i=1}^{N_{LED}}RSS_{direct\ i}(n)+\sum_{i=1}^{N_{LED}}\sum_{j=1}^{N_{multi}(n)}\sigma_{ij}(n)\cdot\rho_{ij}(n)\cdot h(t-\tau_{ij}(n))\right)e^{-j\frac{2\pi kn}{N}} \tag{4}$$

where $RSS(k)$ is the frequency domain signal after FFT, k represents the $k-th$ frequency point, $RSS(n)$ is the collected time domain n-points signal, and N represents the number of points of FFT. It is assumed that the spectrum vector related to the direct reflection path is $RSS(\vec{\alpha})$, the spectrum vector related to the few-times-reflection path is $RSS(\vec{\beta})$, the spectrum vector related to the multipath noise of multiple reflections are $RSS(\vec{\chi})$. Then, the whole spectrum vector can be simplified as follows:

$$RSS(\vec{k})=RSS(\vec{\alpha})+RSS(\vec{\beta})+RSS(\vec{\chi}) \tag{5}$$

We will introduce our observation of the multipath effect and the method of eliminating multipath noise vector $RSS(\vec{\chi})$ interference in Section 5.2.2.

2.4 Absorption Spectrum

This section explicates how alterations in liquid composition impact the absorption spectrum. The interaction between electromagnetic waves and internal components (such as atoms, molecules, and macromolecules) causes phenomena like absorption, transmission, and scattering. This, in turn, leads to a modification in the wavelength [36]. As illustrated in Figure 6, the quantized energy levels of an atom give rise to this phenomenon. When the atom is completely free, it has the lowest energy, called the ground state energy E_0. Under external stimuli such as heat, electricity, or radiation, atoms in their ground state can absorb energy, moving their outermost electron to a higher energy level. This results in the atom becoming excited and transitioning to its excited state. The wavelength and frequency of the atomic absorption spectrum are determined by the energy difference ΔE between the two energy levels that produce the transition: $\Delta E=E_q-E_0=\frac{hc}{\lambda}=h\upsilon$. E_q is the energy of the excited atom, E_0 is the ground-state energy, λ is the wavelength in the spectrum, υ is the frequency, c is the speed of light, and h is the Planck constant. The ground-state atom can transition to the high-energy state E_q only by absorbing light with a frequency of $\upsilon=\frac{E_q-E_0}{h}$. Hence, the spectral line for atomic absorption is also influenced by the atomic structure of elements, and each element has its unique absorption lines. The quantity of spectral lines is directly proportional to the number of atomic energy levels. Suppose the number of atomic energy levels is n, and the ground state is excited to all levels of highly excited states. In that case, the number of atomic absorption spectra that may be generated is $N_{em}=\frac{n^2}{2}$.

Microorganisms can alter the liquid composition and disintegrate specific sections of an element's atomic structure, which results in modifications in the elemental composition. Consequently, the interaction between light and the internal substance is also altered, leading to corresponding changes in the absorption spectrum.

3 Feasibility Study

We verify the proposed model and demonstrate its feasibility with a 3D-printed cup in this section

3.1 Experimental Setup

To verify the feasibility of the model, we used common plastic polymethylmethacrylate (PMMA) in this experiment to print a double-layered cup as the container, as shown in Figure 7. We incorporated a Taptic Engine Vibro-motor underneath the inner cup to generate capillary waves. The inner cup measured 7.3 cm in diameter, 8.1 cm in height, and 1 mm in thickness and had a capacity of 300 ml during vibration. The outer cup had a diameter that was 4 mm

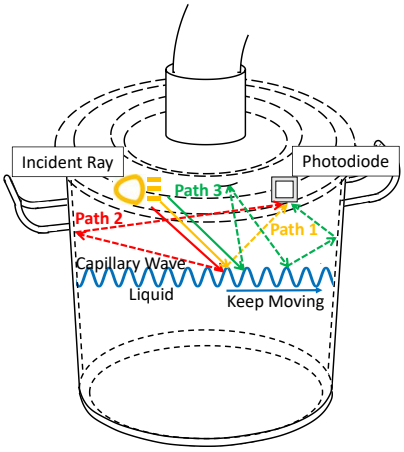

Fig. 5: Multipath propagation model. **Path 1** is the direct reflection path, **Path 2** is the few-times-reflection path related to the capillary wave frequency, and **Path 3** is the multiple reflection paths independent of the capillary wave frequency. Note that there is more than one path for each type of path. We only show one path for each type of path in order not to confuse the figure.

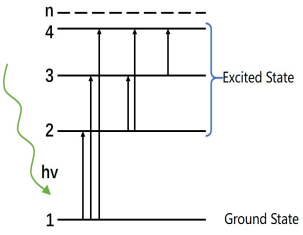

Fig. 6: Absorption Spectrum Model.

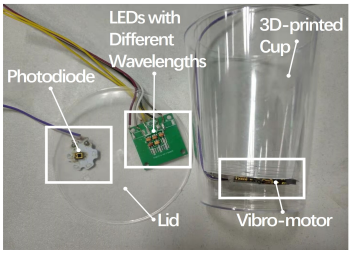

Fig. 7: Container and hardware module for the confirmatory experiment.

larger than the inner cup, and its double-layer structure served to protect it from vibrations. The lid was a 2 mm thick flat plate, and on one side (2 cm away) of the circle center were eleven LEDs mounted alternately with different wavelengths ranging from 940 nm to 1950 nm (940, 1070, 1200, 1300, 1370, 1460, 1550, 1600, 1700, 1850 and 1950 nm). A JK99B surface tension detector and NIR2500 spectrometer measured the surface tension and absorption spectrum (900-2500 nm), respectively. Additionally, a Sysmex-Partec CyFlow Cube 6 flow cytometer (FCM) detector was employed to count the microbes. The sampling rate of the InGaAs photodiode applied for monitoring ranged between 800-2000 nm and was set at 5.6 kHz. The following experiments were performed in a dark room at $25°C$. We conducted experiments on liquids during the aging of four types of wine: red wine (crushed grapes), rice wine (glutinous rice), sake (rice) and spirits (sorghum and corn).

3.2 The effect of Liquid Contamination on Optical Signals

Because it's easier to see liquor deteriorates, we utilized brewed semifinished wine in these experiments and *E. coli*, a common pathogenic microorganism, as a contaminant. We dropped an *E. coli* culture solution (2.7×10^6 cells/ml) into

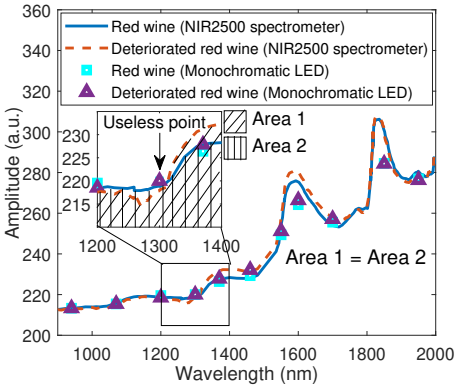

Fig. 8: The monochromatic LED absorption spectrum and the ground-truth spectrum from the spectrometer. Note that the useless point refers to the measurement point where the amplitude change is not obvious due to the non-uniform amplitude changes on its left and right sides.

the four semifinished wines and exposed them to air for 72 hours. We aimed to replicate the microorganisms' contamination during the aging process of wine in a lab setting. Each sample was replicated ten times, and the lid was secured in a separate column to prevent vibration interference. The study monitored the surface tension, reflected light signal under vibrating and static conditions, and the absorption spectrum of the target liquid every 30 minutes. All LED lights were turned on when the vibration started, and the duty cycle was adjusted to 100%. The reflected light signal was then collected for five seconds and converted to the frequency domain, where the most significant peak frequency was identified. The results presented in Figure 9 showed a negative correlation between the surface tension and peak frequency, which was consistent with the simulation model in Section 2.2.

During the next stage, we ceased the vibration and utilized the LED to illuminate each liquid sample for a period of two seconds. Following this, we assessed the intensity of the reflected light collected by the photodiode, which was measured in arbitrary units. We organized the values acquired by each LED in ascending order of light wave wavelength. The reorganized vector was referred to as the LED absorption spectrum. Furthermore, we employed a NIR2500 spectrometer to ascertain the actual ground-truth absorption spectrum. As depicted in Figure 8, the LED absorption spectrum exhibited insensitivity towards liquid decay since the alteration in the absorption spectrum was non-uniform, and specific spectral regions remained unchanged even after liquid decay. However, the ground-truth spectra depicted that when decay occurred, the absorption spectrum underwent crucial changes near 1300 nm, 1400 nm, 1460 nm, 1600 nm, and 1700 nm.

3.3 Deterioration Measurement

We conducted a study to evaluate the deterioration of uncontaminated wines by measuring their surface tension and absorption spectrum after aging for 72 hours. The results showed inconsistencies in the surface tension changes among wines due to differences in raw materials, as shown

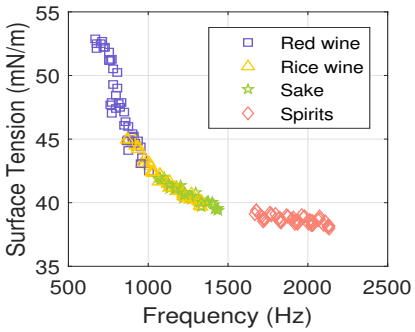

Fig. 9: Variations in the surface tension and reflected signal peak frequency of different wines.

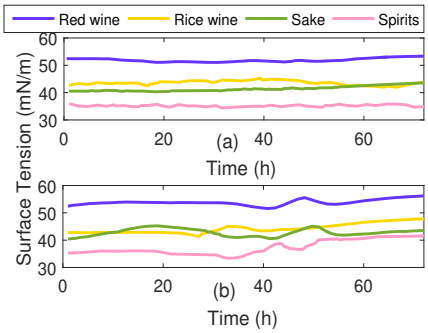

Fig. 10: Surface tension during aging. (a) Uncontaminated wines. (b) Contaminated wines.

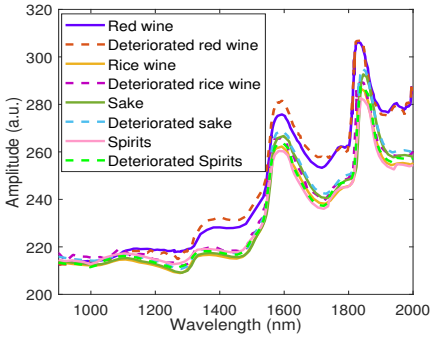

Fig. 11: Absorption spectra of different wines during aging.

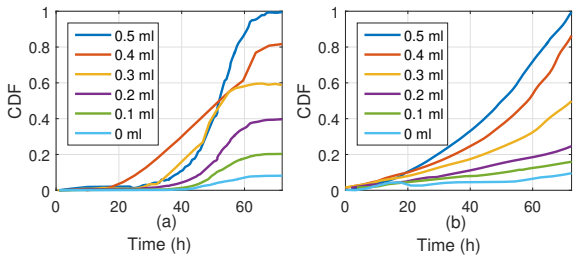

Fig. 12: (a) The surface tension cumulative error. (b) The cumulative error in the absorption spectrum vectors.

in Figure 10 (a). We also assessed The surface tension changes in contaminated red wine samples, and Figure 10 (b) demonstrated fluctuations over time. However, it is challenging to determine the degree of deterioration solely based on surface tension changes since both deteriorated and undeteriorated samples showed identical surface tension values. We propose using other characteristics, such as absorption spectra, to overcome this limitation. Figure 11 illustrates the changes in absorption spectra during the aging process, specifically highlighting significant changes in intensities near wavelengths of 1250 nm, 1400 nm, 1460 nm, 1600 nm, and 1700 nm, indicating a possible correlation with microorganisms and their metabolites.

The modifications in the absorption spectrum and surface tension of contaminated liquors differ significantly from those of uncontaminated ones, as mentioned in Section 3.2. Because of these differences, surface tension and absorption spectra can be utilized to assess the quality of liquor. However, this evaluation criteria may be challenging to establish due to unknown microorganisms' coincident eigenvectors. Moreover, since determining all the microorganisms' features is impractical, feature classification is unsuitable for evaluating liquor quality. Therefore, we suggest a new discrimination approach based on the deviation degree of the featured path. This method takes advantage of the temporal variation of features and transforms the eigenvector into a path that changes over time in high-dimensional space, and measures the deviation degree between the measurement path and the standard path to address this issue.

We first needed to normalize the uncontaminated liquor eigenvectors. We mapped every dimension to the interval $[0, 1]$ and obtained the standard $\vec{L}_{Ref} = [SF_t, AS_i(t)]$, where t is the time, SF is the surface tension value, and AS is the absorption spectrum vector. We set the initial point $\vec{L}_{Ref}(t_0) = [SF_{t_0}, AS_i(t_0)]$ as the reference point and calculated the difference between the measured point and the reference point at each moment $\Delta\vec{L}_{Ref}(t_0) = \vec{L}_{Ref}(t) - \vec{L}_{Ref}(t_0)$. We set the $end - 1$ difference vector $\Delta\vec{L}_{Ref}(t_0)$ from t_0 to t_{end} as the standard path.

We used red wine as the experimental object and set up ten experimental groups. Each group received 1 - 10 drops (0.05 ml/drop) of *E. coli* culture solution (2.7×10^4 cells/ml) and was analyzed every half an hour over a 72-hour period. We used *E. coli*, which is generally used to assess sanitary conditions in food handling environments [37]. In general [37]–[39], an environment is considered very hygienic if the number of Enterobacteriaceae bacteria detected per gram of food is less than 10^2 units. If the number measured is more than 10^4 units, the food poses a health risk. Food in the middle range is unsanitary but does not affect health. In the experiments, the liquid volume was 300 ml. A drop of *E. coli* culture solution was equivalent to a 4.5 cells/ml increase in *E. coli* in the liquors. Liquors contaminated by microorganisms produce substances harmful, such as nitrite, in the body. The World Health Organization Joint Expert Committee on Food Additives (JECFA) stipulates that the daily allowable nitrite intake is 0-0.2 mg/kg·bw [40]. According to research data [41], health impacts occur after deterioration for 14 to 48 hours. If the deterioration time exceeds 72 hours, severe physical discomfort may result from ingesting the food.

We established two measurement tables containing the surface tension and the absorption spectrum data and calculated the contaminated experimental group's relative cumulative variance error based on the uncontaminated control group. Each microorganism has a unique absorption spectrum fingerprint [42], [43], and as they grow, the surface tension changes significantly [24], [25]. Therefore, we used the surface tension and absorption spectra to assess two categories, the contamination time and microorganism content. The contamination time was divided into 12-hour periods, labeled $I - VI$. The microorganism contents were divided into four levels: $Hygiene++$ ($0 - 10^2$ units), $Hygiene+$ ($10^2 - 10^3$ units), $Hygiene-$ ($10^3 - 10^4$ units), $Unhygienic$ (greater than 10^4 units). As shown in Figure 12, just after liquor contamination, the cumulative error in the surface tension was almost 0. However, the cumulative

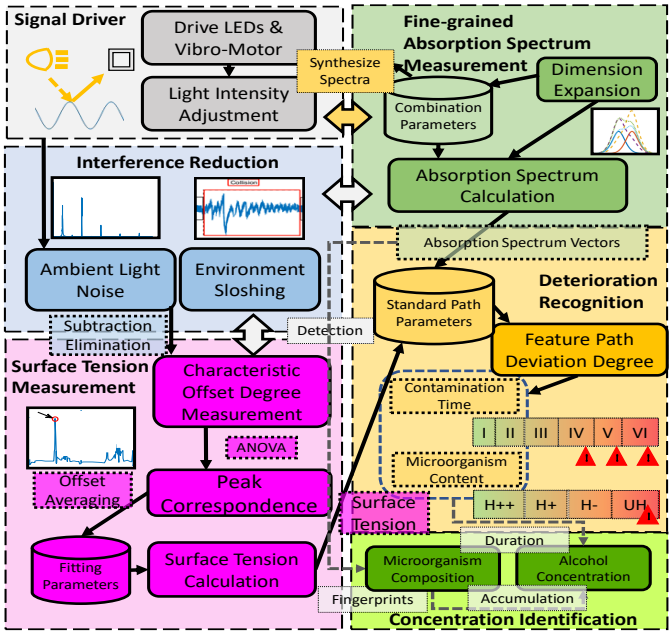

Fig. 13: The workflow of Microbe-Radar.

error in the absorption spectrum vectors increased significantly. Over time, the error increases as more drops of *E. coli* culture solution was added and accelerated. We refer to these cumulative errors as the feature path deviation degree. Using the measurement tables, we determined the degree of liquor deterioration according to the feature deviation. When aging began, we recorded every measurement vector $\vec{L}_{Mea}(t) = [MSF_t, MAS_i(t)]$ and calculated the difference between the measurement vector and the initial point $\vec{L}_{Mea}(t_0) = [MSF_{t_0}, MAS_i(t_0)]$ to obtain the measurement path $\Delta\vec{L}_{Mea}(t_0)$. We calculated the feature path deviation degree by comparing the same time point with the standard path to determine the liquor deterioration degree from the measurement tables.

4 SYSTEM OVERVIEW

Microbe-Radar comprises five modules, as shown in Figure 13.

Signal Drive Module: This particular module governs the motor's vibration, manages the LED drives, regulates the intensity of the light, and concurrently procures the light signal received by the photodiode.

Environmental Interference Reduction Module: During monitoring, this technology module effectively reduces the impact of three types of interferences - ambient light noise, multipath noise, and external vibration interference. In the case of a transparent or opened container, ambient light noise can lead to interference. At the same time, external vibrations from various sources, such as footsteps or knocks, can cause severe disturbance in detection. The module is specifically designed to address these interferences and minimize their impact on detection accuracy.

Surface Tension Measurement Module: This module evaluates the processed light signal, and the current surface tension is subsequently recorded. Further, the deviation in surface tension concerning the baseline signal obtained from the unspoiled liquor is ascertained.

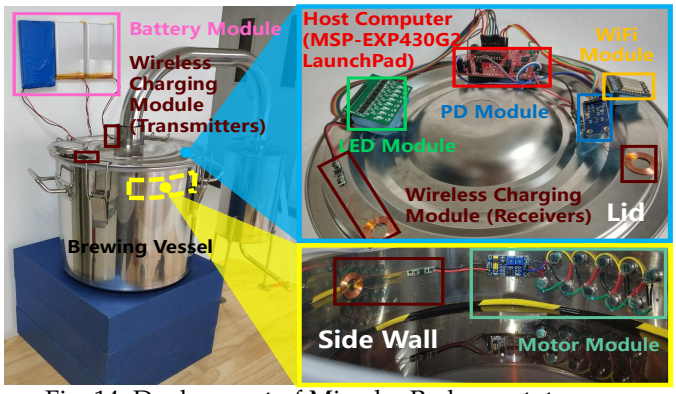

Fig. 14: Deployment of Microbe-Radar prototype on brewing vessel.

Absorption Spectrum Analysis Module: This particular module governs the signal drive module in order to execute a meticulous absorption spectrum analysis. The spectra are then compared with the original liquor's absorption spectrum, and the variance is determined as a result of this comparison.

Deterioration Recognition Module: Upon analysis of surface tension data and absorption spectrum data for the monitored liquor, this module accurately determines the level of degradation based on the type of liquor being monitored. It is evident that the extent of deterioration strongly correlates to the characteristics of the monitored liquor.

5 SYSTEM DESIGN OF MICROBE-RADAR

5.1 Experimental Setup

In Section 3, we presented the absorption spectra of four wines in two undeteriorated and deteriorated states during the aging process. We found that the peaks at wavelengths of 1300 nm, 1400 nm, 1460 nm, 1600 nm and 1700 nm differed the most significantly between the two states. Therefore, we used LEDs emitting at 1070 nm, 1200 nm, 1300 nm, 1460 nm, 1600 nm, 1700 nm, 1800 nm and 1900 nm to cover the peak wavelengths and an InGaAs photodiode, which has an acceptable spectral range of 800–2000 nm. We welded the LEDs and photodiode to two self-designed circuit boards. As shown in Figure 14, a Texas Instruments MSP-EXP430G2 LaunchPad was the host computer, and the sampling rate was set to 5.6 kHz. To ensure data transmission, the host computer was connected to an ATK-ESP8266 WiFi module. The host computer controls the LED module through a pulse width modulator (PWM) connected to GP8101. GP8101 can convert 0-100% duty cycle PWM signals into 0-5 V voltage signals. We designed a spare part, a wireless charging module beside the battery module, which can emit 5 V/500 mA. We installed the host computer, LED module, photodiode module, WiFi module, battery module and wireless charging module on the brewing equipment's lid. Ten B1036F1 vertical linear motors were installed on the brewing vessel wall to generate capillary waves controlled through the NE555 pulse generator. They are all covered with a layer of waterproof nanospray. We tested the system with different materials in small industrial brewing equipment at room temperature ($25°C$), including stainless steel, wood, glass and ceramics, and volumes of 12 L, 22 L, 36 L and 50 L. Simultaneously, we used a JK99B surface tension

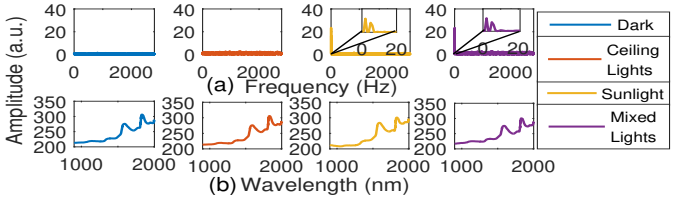

Fig. 15: Ambient light interference.
(a) Amplitude-frequency diagram for the photodiode.
(b) The environmental spectrum of the spectrometer.

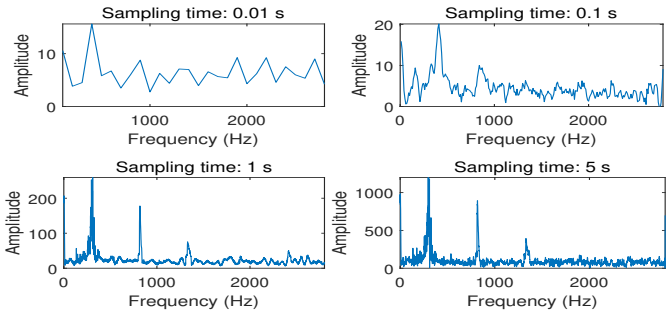

Fig. 16: Signal spectrum of different sampling time.

detector, a NIR2500 absorption spectrometer, and a Sysmex-Partec CyFlow Cube 6 flow cytometer (FCM) to measure the ground-truth data, and the cost of each was approximately $5,000, $15,000, $8,000, respectively.

5.2 Interference Elimination

5.2.1 Eliminating Ambient Light Noise

Manufacturers can use light-transmitting materials like glass as containers or lids to make it easier to observe the aging process. However, this can lead to noise from ambient light radiation due to sunlight, light bulbs, and other surrounding lights. To counter this, we utilized Microbe-Radar's photodiode and spectrometer to gather data in three different experimental settings: an office, a conference room, and a laboratory, wherein the ceiling lights were T8 fluorescent lights. Our recordings were taken under four different conditions, namely dark, sunlight, ceiling lights, and mixed lights. It is crucial to account for these factors while conducting experiments requiring precise light signal measurements.

Based on the data shown in Figure 15, the photodiode signal exhibited minimal noise levels in both the dark and ceiling light scenarios. The signal spectrum also remained flat and at a low amplitude. However, when exposed to sunlight, the photodiode detected low-frequency noise with a relatively high amplitude, leading to fluctuations in the signal spectrum. To reduce errors caused by environmental interferences, it is imperative to eliminate these interferences. In order to achieve this, Microbe-Radar opts to turn off the LEDs and calculates the average ambient light amplitude-frequency curve before detection. Once in the test phase, Microbe-Radar subtracts the ambient light amplitude-frequency curve from the signal.

5.2.2 Eliminating Interference from Multipath Noise

Through the vibration, the capillary wave produced by the liquid surface perpetually moves forward. The direct reflection path results from a convex wave having only one reflection path, meeting the reflection law. Certain few-time-reflection paths have specific path propagation principles. Hence, the direct reflection path and particular few-time reflection paths are time-dependent determinants. However, several irregular multiple reflection paths or multipath noise represents time-independent random processes. Increasing the sampling time can intensify the randomness of multipath noise to ensure unstable and weak multipath noise gets attenuated. Nonetheless, Microbe-Radar strives for real-time perception. For such purposes, signal acquisition time would require shortening to achieve real-time perception and reduce computational efforts. This determines the appropriate sampling time necessary through experimental observation.

Observation: The vibration reached a steady state after the first 2 s. We fixed the lid to prevent the interference of lid vibration, collected signals of different time lengths (i.e., 0.01 s, 0.1 s, 1 s, 5 s), and obtained the spectrum by FFT. As shown in Figure 16, we found that when the sampling time is short (e.g., 0.01 s and 0.1 s), the resolution of the signal spectrum is low, and there are some prominent and uncertain peaks at many frequency points, even at high frequencies. However, when the sampling time is long enough (e.g., 1s, 5s), the signal spectrum has only three obvious peaks, which tend to be stable, and no obvious peaks are located at frequencies higher than 1500 Hz. These observations show that when the sampling time is short, the peak value of multipath noise in the frequency domain is accidental, and the signal samples are not ergodic. That is, the signals' mean value and autocorrelation function are unstable. Only when the signal acquisition time is long enough the multipath noise independent of the capillary wave frequency will tend to be stable in the spectrum. At this time, the direct reflection path spectrum and the few-times-reflection path spectrum related to the capillary wave frequency will not be covered by the multipath noise. The experimental results in Figure 16 preliminarily prove that our intuition is correct. We choose 1 s as the sampling time, which is enough to avoid the interference of multipath noise.

Analysis: To help understand and justify our approach, we analyzed the signal in terms of spectrum distribution and temporal correlation based on the multipath model of Section 2.3. The vibration reached a steady state after the first 2 s. We fixed the lid to prevent the interference of lid vibration, collected three 1 s-long signals with different starting times, and performed FFT to obtain the spectrum RSS_1, RSS_2 and RSS_3 (Figure 17 (a)).

(1) Spectrum distribution. First, when the capillary wave propagates forward, the multipath noise will undergo multiple reflections and superposition, so the multipath noise spectrum $RSS(\vec{\chi})$ (gray part in Figure 17 (a)) has no obvious regularity. On the contrary, the change speed of the direct reflection path and the few-times-reflection path is much smaller, so the direct reflection path spectrum $RSS(\vec{\alpha})$ (208–395 Hz in Figure 17 (a)) and the few-times-reflection path spectrum $RSS(\vec{\beta})$ (758–862 Hz and 1279–1391 Hz in Figure 17 (a)) are concentrated in the low-frequency part. Moreover, the frequency of the direct reflection path is lower than that of the few-times-reflection path. Secondly, the multipath noise independent of capillary wave frequency attenuates

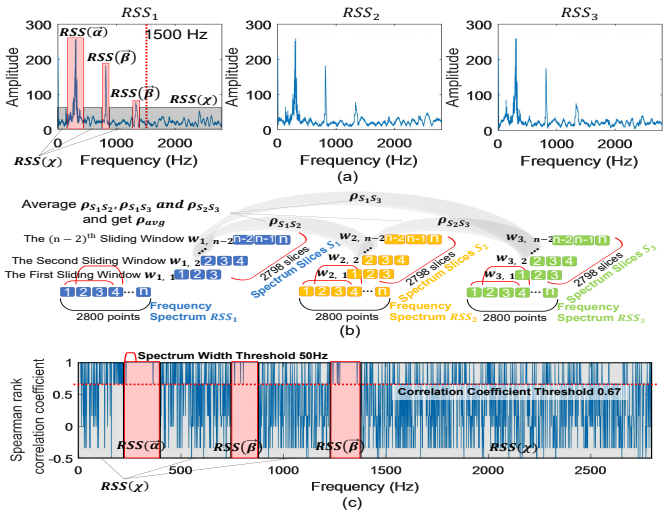

Fig. 17: (a) Three signal spectrums with different sampling start times. (b) The schematic diagram for calculating the average cross-correlation coefficient vector of three segment signals. (c) Average cross-correlation coefficient vector.

obviously after multiple reflections, so the amplitude of the multipath noise spectrum $RSS(\vec{\chi})$ is small. Instead, the amplitude of the direct reflection path spectrum $RSS(\vec{\alpha})$ and the amplitude of the few-times-reflection path spectrum $RSS(\vec{\beta})$ are large.

(2) Temporal correlation. The temporal correlation of multipath noise is weak, so the multipath noise spectrum $RSS(\vec{\chi})$ fluctuates in temporal correlation and contains small values. Instead, direct reflection path spectrum $RSS(\vec{\alpha})$ and few-times-reflection path spectrum $RSS(\vec{\beta})$ does not change significantly with time, so direct reflection path spectrum $RSS(\vec{\alpha})$ and few-times-reflection path spectrum $RSS(\vec{\beta})$ have large time correlations. We analyzed the temporal correlation of the spectrum by calculating the cross-correlation coefficient between the signal spectrums sampled at different starting times. The calculation diagram is shown in Figure 17 (b). We divided the three n-points ($n = 2800$, $length = 1s$) spectrums (RSS_1, RSS_2 and RSS_3 shown in Figure 17 (a)) into slices with the sliding window of 3 points and the sliding step of 1 point, respectively, to generate $3 \times (n-2)$ spectrum slices S_1 ($w_{1,1}$, $w_{1,2}$, $w_{1,3}$,..., $w_{1,n-2}$), S_2 ($w_{2,1}$, $w_{2,2}$, $w_{2,3}$,..., $w_{2,n-2}$) and S_3 ($w_{3,1}$, $w_{3,2}$, $w_{3,3}$,..., $w_{3,n-3}$). Then we calculated the Spearman rank correlation coefficient vector between these spectrum slices to obtain $\rho_{s_1s_2}$, $\rho_{s_1s_3}$ and $\rho_{s_2s_3}$ ($3 \times (n-2)$ values), and finally took the average vector of the three correlation coefficient vectors ρ_{avg} ($length = (n-2)$). We got the correlation coefficient vector as shown in Figure 17 (c). Note that the length of the correlation coefficient vector is 2798 and the spectral range is 1–2798 Hz. We found that the correlation coefficient of the multipath noise spectrum $RSS(\vec{\chi})$ (the gray part in Figure 17 (c)) fluctuates constantly. Instead, direct reflection path spectrum $RSS(\vec{\alpha})$ (225–381 Hz in Figure 17 (c)) and few-times-reflection path spectrum $RSS(\vec{\beta})$ (756–866 Hz and 1273–1396 Hz in Figure 17 (c)) have large correlation coefficients. Note that we calculated the Spearman rank correlation coefficient instead of the Pearson correlation coefficient. On the one hand, the distribution of the sliding window data of the three points

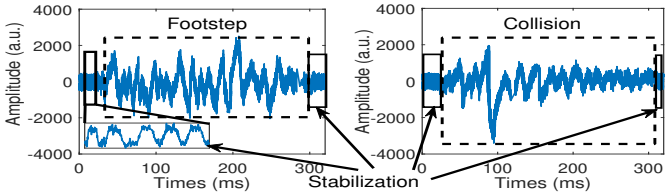

Fig. 18: Interference from footsteps and collisions from people nearby on the time-domain signals.

is difficult to describe, and the Spearman rank correlation coefficient does not require the distribution form of two variables, providing a more conservative estimate. On the other hand, the Spearman correlation coefficient is rank-dependent, so the correlation coefficient can be divided into multiple levels to facilitate observation and analysis.

The corresponding spectrum ranges obtained from analysis of the above two aspects are similar, which shows that the multipath noise tends to a small value in the spectrum and has no obvious distribution law, and the multipath noise spectrum is time-independent. Therefore, it is reasonable for us to increase the sampling time to randomize and attenuate the multipath noise. Note that although we have also roughly found the range of direct reflection path spectrum $RSS(\vec{\alpha})$ and few-times-reflection path spectrum $RSS(\vec{\beta})$ related to the capillary wave frequency through the above analysis, we cannot know the precise and fine-grained frequency points. In addition, we have not eliminated the interference caused by the lid vibration. Therefore, we introduced in detail the method of extracting frequency points related to capillary wave frequency in Section 5.3.

5.2.3 *Reducing Interference from Sloshing*

The motion generated by an external force acting on the liquid in a container causes it to slosh, interfering with accurate measurements. Despite the differences between this inertial motion and the motion of liquid capillary waves, the resulting interference can disrupt the equilibrium in the liquid surface tension and hinder capillary wave generation. As a result, it is crucial to minimize the steps and collisions of people near the container. This force disrupts the equilibrium of the liquid surface tension, resulting in interference with capillary wave production. As a result, the objectivity of the measurement can be compromised.

The footsteps and collision interference received by Microbe-Radar's photodiode are depicted in Figure 18. These interferences caused significant long-lasting amplitude changes because inertial motion creates a large specular reflection on the surface of the liquid. By analyzing the capillary wave reflected light signal, we discovered a stable period T, in which the sum of the amplitudes during that period remained constant. We determined that T lasted approximately 2 ms. We calculated the average amplitude $\bar{A} = \frac{1}{T}\sum_{t=0}^{T} I_t$. Then, we searched for a significant long-lasting amplitude change. After setting the period average as the dividing line, we calculated the amplitude and $S = \sum_{t=(n-1)T}^{nT} |I_t - \bar{A}|, n \in \mathbb{Z}^+$ within the period. We determined whether sloshing interference occurred by setting the

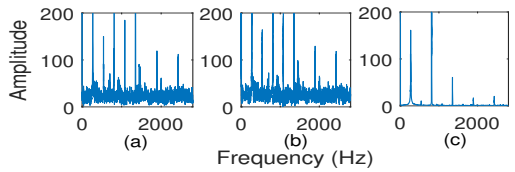

Fig. 19: (a) & (b) Different surface tension signals during vibration. (c) Signal when the lid was fixed.

threshold δ for the sum of the amplitudes S. By suspending the measurement for 30 s, we avoided this interference.

5.3 Surface Tension Calculation

5.3.1 Challenge

In Section 2, we introduced how LEDs can measure surface tension by reflecting capillary waves, and the model was verified in Section 3. However, we encountered a challenge when we applied the system to brewing equipment. As shown in Figure 19 (a), the LED reflected light signal had tremendous noise, making it difficult to directly observe the frequency offset even when the surface tension increased, as shown in Figure 19 (b). Since the brewing equipment was not double-layered like the 3D-printed cup in Section 3, vibration from the container wall affected the lid even if it was fixed to a separate column. Therefore, the LED and photodiode modules interfered with the vibration and produced considerable noise when the motor generated the capillary waves. However, traditional filters are not suitable for this complex frequency noise elimination because the masked feature seems to be noise and would be filtered out.

5.3.2 Observation

The original frequency offset was challenging to find with complex frequency noise in the signal. We experimented with four types of wine, with 15 samples of each type (10 with different surface tensions + 5 with the same surface tension). We collected each sample for 10 seconds. A characteristic can be separated if its distribution is distinct from the noise's. Therefore, we used 1 second as the window to observe the signal fluctuation law in the frequency domain among all samples. We calculated the variance for all frequency points. For convenience in expression, the variance for the same sample, the samples with the same surface tension, and the samples in different surface tension groups were named self-variance distribution, intragroup variance distribution, and intergroup cross-variance distribution.

The self-variance distribution and the intragroup variance distribution had almost the same frequency point variance distribution. These distributions were relatively similar even if the surface tension was different. However, there were considerable differences in the intergroup cross-variance distribution. The observations show that the signal difference came from the change in surface tension related to the capillary wave reflection signal. Therefore, these reflections can be decomposed into the noise caused by vibration and the characteristics of capillary wave reflection.

5.3.3 Measurement of the Characteristic Offset Degree

This section introduces the method of finding the frequency offset. Figure 20 shows the simplified solution. The characteristic frequency offset is superimposed with the vibration noise because of the independence of the noise from the characteristic frequency. It is unrealistic to find the characteristic offset directly from the superimposed signal. However, if we calculate the absolute value of the difference between the two signal frequency curves, we obtain two apparent peaks in the frequency domain. Moreover, the distance between these two peaks is the characteristic frequency offset.

We regard the disturbance caused by white noise as the standardized normal distribution e_{tij}. The surface tension of a liquor in its initial state was used as the reference, so we consider the reference amplitude at each frequency point as $A_{t_0ij} = a_{t_0ij} + e_{t_0ij}$. A_{t_0ij} is the amplitude at frequency point j during the sequence i measurement at time t. a_{t_0ij} is the theoretical value for the initial state $t = t_0$, and e_{t_0ij} is the white noise of the normal distribution. Because the frequency offset causes more amplitude changes than the noise, we can divide the signal into three parts, $A_{tij} = a_{t_0j} + a_{tj} + e_{tij}$. Among them, a_{tj} is the disturbance caused by the measurement. In the detection, if a_{tj} can be regarded as 0, we believe this frequency point does not have frequency offset characteristics. Therefore, we used analysis of variance (ANOVA) to infer this point, assuming that a_{tj} can be regarded as 0. We collected ten samples and put them into the same group each time to calculate the random error at each frequency point.

To explain this clearly, we assume that ten samples are taken at time T, and each sampling lasts for 10 seconds. At this time, the random error of the frequency point can be expressed as $SS_e = \sum_t \sum_{i=1}^{10} \left(A_{tij} - \bar{A}_{ij}\right)^2, t = t_0, T$. Next, we compare with the liquor at $t = t_0$ to calculate the global deviation $SS = \sum_t \sum_{i=1}^{10} \left(A_{tij} - \bar{A}_j\right)^2, t = t_0, T$. The sum of the squares of the difference between the signal levels at time T is $SS_T = SS - SS_e$. We substitute the degrees of freedom and get $MS_T = \frac{SS_T}{k-1}, MS_e = \frac{SS_e}{n-k}$. We need to use the F-test to determine whether to accept the null hypothesis $\frac{MS_A}{MS_e} \leq F(\alpha)$.

As shown in Figure 21, we found offset frequency points between two samples with different surface tensions. The figure shows that there is more than one characteristic point resulting from the reflected light having different multipaths. Moreover, each peak representing the characteristic has another peak with a similar curve profile. This similar curve comes from the offset of the characteristic frequency. Therefore, we need to calculate the frequency difference between these corresponding characteristics.

To reduce the computational complexity, we used these two characteristics to find the frequency offset: the corresponding characteristic has a similar peak curve, and the frequency offset generated by any characteristic is approximate. We considered the peak point spacing within the threshold τ s the same peak curve and selected the peak at the median to represent the peak curve. Assuming that there are n peaks, we calculated the peak difference and frequency offset between all the peaks to obtain a matrix with a diagonal of 0, $\begin{bmatrix} \left(\Delta_0^0 A, \Delta_0^0 F\right) & \dots & \left(\Delta_0^{n-1} A, \Delta_0^{n-1} F\right) \\ \vdots & \ddots & \vdots \\ \left(\Delta_{n-1}^0 A, \Delta_{n-1}^0 F\right) & \dots & \left(\Delta_{n-1}^{n-1} A, \Delta_{n-1}^{n-1} F\right) \end{bmatrix}$.

We first selected the element $\Delta_0^i A$ in the first row from

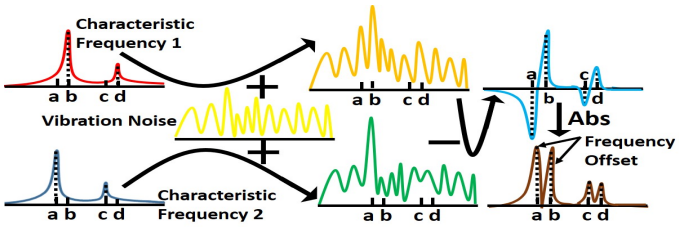

Fig. 20: The solution of the characteristic offset.

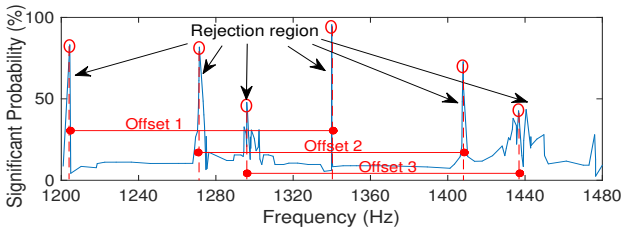

Fig. 21: Frequency offset points found by ANOVA.

the non-diagonal elements and occupy column i. Then, $\Delta_0^i F$ was taken as the reference frequency offset. After that, we selected the non-diagonal element in other rows with three principles: ΔA was close to 0, the difference between ΔF and $\Delta_0^i F$ was close to 0, and the column was not occupied. After finishing the selection, we calculated all the selected element frequency offset variances $V_{\Delta F}$. Moreover, after traversing all elements in the first row, we chose the combination with the minimum variance $V_{\Delta F}(i) = \min\{V_{\Delta F}(m) | m \in [0, n-1]\}$. We averaged the frequency offset of all elements $\left\{\Delta_j^k F | (j,k) \in V_{\Delta F}(i)\right\}$ and then obtained the characteristic offset.

To verify the effectiveness, we expanded the method to other liquor experiments. We selected four kinds of liquors in Section 5.1 and calculated the average of the offset frequency point interval under 40 surface tension states. We analyzed the correlation between the value and the change in surface tension and calculated the Pearson correlation coefficient. The average Pearson correlation coefficient for the four liquors was greater than 0.9, indicating a significant correlation. To accurately calculate the change in surface tension, we established the corresponding relationship between the characteristic offset and the ground-truth surface tension change and used the least squares method to obtain the fitting function. In Section 3.3, we revealed that only the surface tension change needs to be monitored to assess the degree of liquor deterioration. However, the initial surface tension can be added to the surface tension change calculated from the fitting function to determine the real surface tension.

5.4 Fine-Grained Absorption Spectrum Measurement

5.4.1 Limitations of the LEDs

Although the surface tension change can be used to identify liquor deterioration, some liquors may have the same surface tension even at different degrees of deterioration. Since deterioration involves decomposing the liquor and metabolite production by microorganisms, the material composition changes. From Section 2.4, which introduced the physical model of the absorption spectrum, we know that the absorption spectrum differs on the basis of these changes in material composition.

However, the metabolite alterations made by microorganisms are subtle. Microbe-Radar comprises only LEDs, so measuring a fine-grained absorption spectrum is challenging, as LEDs can provide only a narrowband spectrum optical signal. When the detected object absorbs part of the light spectrum, we will obtain only an intensity value through the photodiode. The difference between this light intensity and the intensity of the light emitted from the original LED results in a coarse-grained absorption spectrum. However, within this waveband range, as long as the absorption spectrum area does not change, the coarse-grained absorption spectrum will not differ. Because of subtle changes in the absorption spectrum coupled with the noise from the system components, obtaining the same absorption spectrum area for different materials is common. Therefore, limited by the LED narrowband spectrum, it is difficult to detect subtle changes in the absorption spectrum with the photodiode.

5.4.2 Observation

To detect a fine-grained absorption spectrum with traditional methods, the emission waveband must be narrow, the band must be higher than what is traditionally used, and a more extensive spectral range must be observed. In short, the resolution must be increased. There are two methods to achieve this goal: use expensive dispersive elements and sophisticated detectors such as spectrometers or use more light sources with different wavelengths and extremely narrow bands (such as lasers). However, these methods are expensive. If the reflected spectrum can be displayed in different dimensions, we can reduce the interference with the same absorption spectrum area and achieve a fine-grained inspection.

We first analyze the LED. The spectral radiation distribution of the LED is not a strictly symmetrical Gaussian distribution [44]. The peak wavelength's left end fits a Gaussian distribution function, and the right end fits a piecewise function of the Lorentz distribution function. Therefore, the LED spectrum can be simplified as $I(\lambda) = \alpha I_0 \times \exp\left[c_1\left(\frac{\lambda-\lambda_0}{\Delta\lambda}\right)^2 \times \exp\left(c_2\left|\frac{\lambda-\lambda_0}{\Delta\lambda}\right|\right)\right]$. $I(\lambda)$ is the intensity of radiation from an LED in the optical axis direction, λ is the incident wavelength, α is the current conversion coefficient, I_0 is the drive current, λ_0 is the center wavelength, $\Delta\lambda$ is the full width at half maximum (FWHM), and c_1 and c_2 are constants.

We found that the FWHM of the LED spectrum was not constant from measurements. As shown in Figure 22 (a), the original FWHM was 90 nm. Then, the drive current was increased from the original 10 mA to 50 mA while maintaining the operating voltage at 5 V. As the current increased, the FWHM of the LED spectrum gradually expanded. Therefore, increasing the current can cover wavebands beyond the original LED waveband.

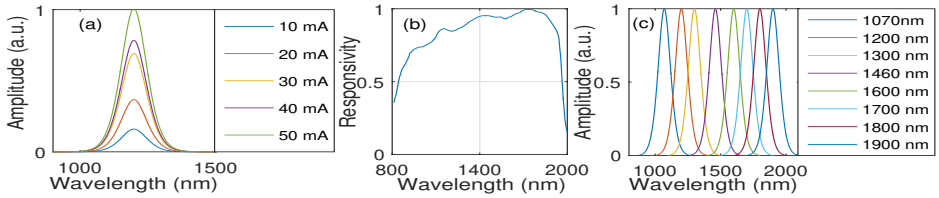

Fig. 22: (a) LED spectrum expand. (b) The relative spectral responsivity of Microbe-Radar's photodiode. (c) The spectral distribution of Microbe-Radar's LEDs.

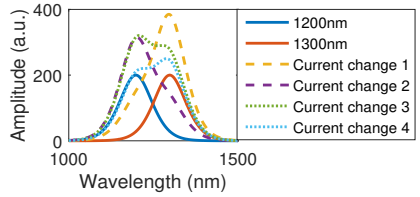

Fig. 23: Spectrum synthesized example.

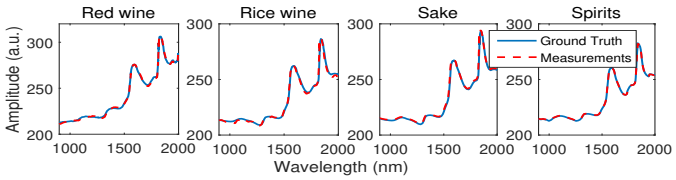

Fig. 24: The absorption spectrum calculated from LEDs.

5.4.3 Dimension Expansion of a Coarse-Grained Absorption Spectrum

In this section, we introduce how to expand the dimensions of a coarse-grained absorption spectrum. In brief, if the lights used to analyze a liquor have different spectral profiles, then subtle changes in the absorption spectrum will result in a different reflectance spectrum. Therefore, lights with different spectral profiles represent different dimensions of information. However, we must also consider the photodiode characteristics to measure these profile changes. Due to the photoelectric effect, the light of different wavelengths can excite different photons in the PN junction and generate varying numbers of electrons. Therefore, the photodiode sensitivity changes. Figure 22 (b) presents a curve of the relative spectral responsivity of Microbe-Radar's photodiode. We took advantage of the various responsivities of photodiodes to different light wavelengths and combined LEDs to achieve a signal sensitive to subtle changes in the absorption spectrum. Considering the LED waveband scalability presented in Section 5.4.2, we can superpose two different waveband spectra to obtain different spectral profiles for the lights. Moreover, adjusting the current leads to many available combinations, and these spectra will have a different center wavelength from the LED's original.

Therefore, LEDs should have several characteristics. First, the wavebands of all LEDs should overlap with the detection frequency. Second, each LED spectral waveband should overlap with the others. Therefore, we selected eight LEDs with different wavelengths, as shown in Figure 22 (c). Because of their different internal structures, they had diverse luminous intensities and FWHMs.

Next, we introduce the method of generating the narrowband spectrum. Because the photodiode's ability to generate photons is limited, it will become saturated if the spectrum exceeds the threshold. At this time, regardless of the absorption spectrum changes, the current received will remain stable. Therefore, the emitted light intensity must be within the receiving range, which is the first constraint. To be conservative, we set the total light intensity of the synthesized spectrum to be less than or equal to the photodiode's receiving threshold.

In addition, we need to consider the different reflective properties of each liquor. Therefore, we need to detect the reflection coefficient of the liquor first. We started each LED at the maximum allowed current and reduced it until the photodiode value changed. Then, we stopped decreasing the current and recorded the value $MaxI_\lambda$ as the maximum detection current for the given LED. Taking into account the rationality of the setting, we also need to remove useless amplification. If all LEDs of the same wavelength have the same amplification factor ratio for any two combinations of LEDs, then these two combinations are essentially the same, and one of them can be eliminated. Therefore, $TI_n = \sum_i \left[L_i\left(\lambda, {}^nk_\lambda\right) - PL - AS_\lambda\right] \cdot R_\lambda$, and we can determine all the constraints:

$$s.t. \begin{cases} TI_n \le Threshold_{PD} \\ {}^nk_\lambda I_\lambda \le MaxI_\lambda \\ \forall \left\{{}^nk_\lambda\right\} \ne \alpha \left\{{}^mk_\lambda\right\}, m \ne n, \alpha \in \mathbb{R}^+ \end{cases} \tag{6}$$

TI_n represents the total light intensity of the nth combination in the photodiode, which is the reflected light intensity multiplied by the responsivity R_λ. The reflected light intensity combines the LED light intensity $L_i\left(\lambda, {}^nk_\lambda\right)$, path loss PL , and absorption spectrum AS_λ. Each LED current may enlarge k_λ times the working current I_λ but should be less than or equal to the maximum current $MaxI_\lambda$. α is a positive real number. We set k_λ's step size to be 0.05 to calculate all the combination sets of k_λ for any two LEDs with overlapping wavelengths. Figure 23 shows some of the narrowband spectra produced by two LEDs with overlapping wavelengths.

After determining the combination of LED current values, we formulated each LED power sequence and current change. Then, we used a photodiode to record each reflected light value, thereby obtaining the dimensional expansion of the coarse-grained absorption spectrum. We substituted all the known values into TI_n and simultaneously $I\left(\lambda\right)$, used the Gaussian elimination method, built an augmented matrix, and solved the matrix with elementary row transformation. By solving the determinant, we obtained accurate absorption spectrum values. As shown in Figure 24, we compared the absorption spectra calculated from LEDs with the ground truth, and the mean absolute percentage error (MAPE) was only 0.7%.

6 SYSTEM EVALUATION

6.1 Liquor Monitoring Performance

6.1.1 Measurement Accuracy for Different Liquors

To verify Microbe-Radar's performance in liquor monitoring, Microbe-Radar monitored the aging process of different wines (red wine, rice wine, sake, and spirits) for 72 hours.

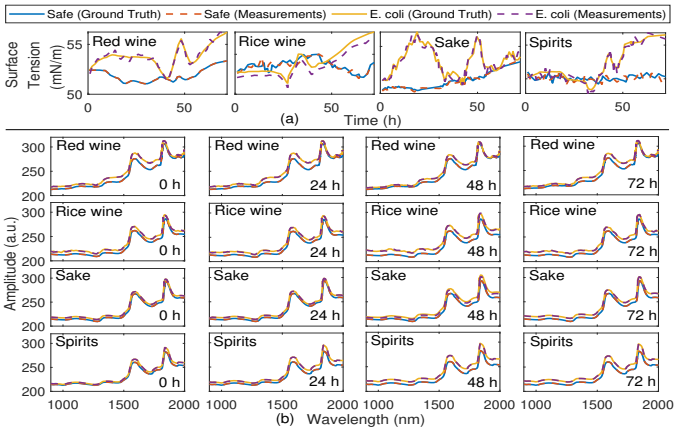

Fig. 25: (a) Surface tension and (b) absorption spectra of different liquors measured by Microbe-Radar.

We divided the experiment into two groups: a normal aging group (the safety group), and a group contaminated with *E. coli* culture solution before aging (*E. coli* group). Before starting, we poured the wines into containers and maintained 25 cm between the liquid surface and the monitoring module. After measuring the initial surface tension and absorption spectrum, we input the data into Microbe-Radar's database and began monitoring. The surface tension and absorption spectrum curves measured by Microbe-Radar in Figure 25 are very close to the ground-truth data. The surface tension of the safety group changed relatively smoothly, unlike that of the *E. coli* group, which fluctuated widely. The absorption spectra of these two groups contained large fluctuations but were all concentrated on different wavebands. For the 72-hour monitoring period, the mean error in the liquid surface tension in the safety group was only 0.89 mN/m, while the mean error for the *E. coli* group was 1.16 mN/m. The mean absolute percentage error (MAPE) of the absorption spectra of the safety group and *E. coli* group was 2.37% and 3.04%, respectively.

6.1.2 Measurement Accuracy for Different Pathogenic Bacteria

To verify the monitoring ability of Microbe-Radar for different pathogenic bacteria, we replaced *E. coli* with Salmonella and Staphylococcus aureus under the same experimental conditions as in Section 6.1.1. We calculated the mean error of surface tension and MAPE of the absorption spectrum during the 72-hour monitoring. As shown in Figure 26, Microbe-Radar can accurately monitor *Salmonella* and *Staphylococcus aureus (S. aureus)* contamination with very low error.

6.1.3 Measurement Accuracy with Different Container Volumes

The results for different container volumes are shown in Figure 27. As the volume increased, the surface tension error first decreased and then increased again. Initially, the interference caused by vibration decreased. However, as the volume increased, the container thickness also dramatically increased, and the capillary wave generated by the vibromotor vibration decreased, which increased the interference caused by noise. The surface tension errors with the four container volumes were 0.89, 0.71, 0.65, and 1.24 mN/m, while the MAPE of absorption spectra did not obviously change: 2.31%, 2.40%, 2.36%, and 2.47%, respectively.

6.1.4 Measurement Accuracy with Different Container Materials

Considering that different merchants will use different container materials, we tested four container materials (stainless steel, wood, glass, and ceramics) for spirits aging. Of the four types of containers shown in Figure 28, wood resulted in the worst performance, as the rigidity of wood materials is low and absorbs vibration energy. The low energy transmission causes the liquid capillary wave to decay quickly, which leads to significant measurement errors.

6.1.5 Surface Tension Measurement Boundary

We found relatively big errors when Microbe-Radar measured the liquids with too large or too small surface tension, which showed that Microbe-Radar's surface tension measurement had upper and lower limits. On the one hand, when the liquid surface tension is too small, there are more capillary waves in the receiving range of the photodiode, and the multipath noise of capillary waves is more obvious. The path related to the frequency of capillary waves received by the photodiode will be covered by multipath noise. On the other hand, when the liquid surface tension is too large, the capillary wave is a very gentle sine wave, and its reflected light is difficult to cause the change of photodiode receiving intensity. We determine Microbe-Radar surface tension measurement's upper and lower limits by error threshold method [23]. Specifically, if the Microbe-Radar measurement error exceeds 1.5 mN/m, it means that the measurement boundary is reached. We prepared different concentrations of alcohol solution and NaCl solution to cover the surface tension range of 20–90 mN/m and recorded the measurement errors of surface tensions. As shown in Figure 30, when the surface tension is less than 28 mN/m or greater than 81 mN/m, the error exceeds 1.5 mN/m, indicating that the accurate measurement range of Microbe-Radar is 28–81 mN/m.

6.2 Liquors Quality Determination

6.2.1 Baseline

In Section 3.3, we set up two criteria for liquor quality based on the number of microorganisms and contents of metabolites that affect human health: the duration of contamination and the microorganism content. We took 40 samples of each of the four types of wine. The results in Figure 29 reflect a mean recognition accuracy rate of 95.1%. The accuracy of identifying categories that impact health (greater than IV, $Unhygienic$) was 97.5%. This means that Microbe-Radar can accurately identify the deterioration of liquor and prevent food safety accidents.

6.2.2 Daily Beverages Deterioration Warning

Microbe-Radar can not only be applied to the brewing industry but also be used to monitor the deterioration of daily beverages because of Microbe-Radar's ability to monitor the changes in liquid surface tension and absorption spectrum. After drinking or being exposed to the air for a period of time, the bacteria in the mouth or the air will enter

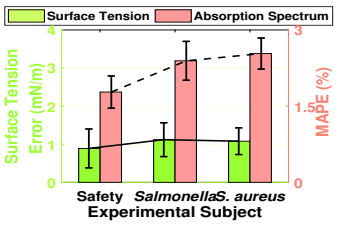

Fig. 26: The measurement results for different pathogenic bacteria.

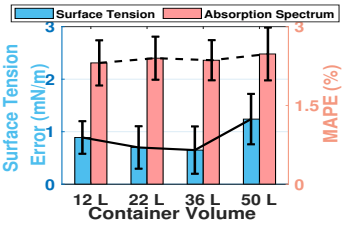

Fig. 27: The measurement results for different container volumes.

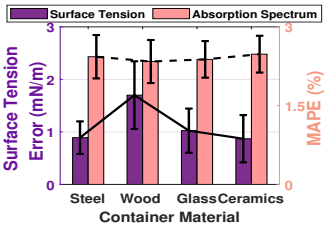

Fig. 28: The measurement results for different container materials.

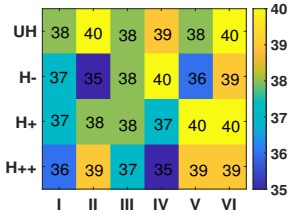

Fig. 29: Liquors quality determination.

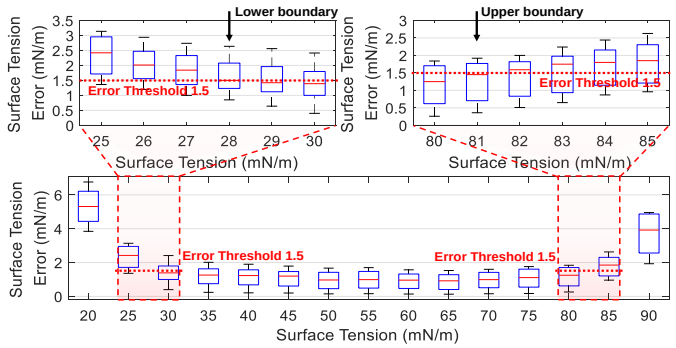

Fig. 30: Exploring Microbe-Radar's surface tension measurement boundary.

the beverages, and the sugar, protein, and other nutrients in the beverages provide suitable conditions for the rapid propagation of bacteria. It is difficult and inaccurate to judge the deterioration of beverages only by their appearance and smell. However, if the cup's daily life is equipped with a Microbe-Radar system, the cup can monitor the bacterial content of the beverages (e.g., milk, milk tea, fruit juice, vegetable juice) in real-time, and tell people whether the beverages are suitable for drinking. We used the 3D-printed cup in Section 3.1 for experiments because it was closer to the shape of the daily cup. We expanded the subjects to various beverages of multiple brands (i.e., 4 kinds of milk, 3 kinds of milk tea, 4 kinds of orange juice, 4 kinds of apple juice, and 3 kinds of tomato juice). The samples of deteriorated and undeteriorated beverages of each brand were 8, respectively. We used a method similar to the method in Section 3.3 to judge the deterioration degree of the beverages. In the laboratory at 25 °C and 94.7% RH, we took 300ml of each beverage immediately after opening and measured the surface tension and absorption spectrum. At the same time, we assumed that the liquid surface tension and absorption spectrum of the uncontaminated beverage remained unchanged within 72 hours, which was taken as the standard path of the control groups. Then one of our researchers sipped each beverage and added 300ml of the drunk (contaminated) beverages to the cup. Then, we recorded the relative cumulative variance error of the liquid surface tension and the liquid absorption spectrum relative to the standard path within 72 hours to obtain the deviation degree of the characteristic path. It is worth noting that the microbial content of unopened beverages will hardly change, which is different from liquor. At the same time, we used Sysmex-Partec CyFlow Cube 6 flow cytometer to record the content of *E. coli* every 6 hours. When the level of microbial content reached $Unhygienic$, we believed that the beverages were no longer suitable for drinking. We recorded the characteristic path deviations of the surface tensions and the absorption spectrum vectors at that time as the thresholds of the beverages' deterioration warning. As long as one of the characteristic path deviations of the surface tension or that of the absorption spectrum exceeded the threshold, we considered that the beverage had deteriorated. As a binary classification problem, deterioration warning has the following four results: True Positive (TP), positive samples are correctly classified as positive; False Positive (FP), negative samples are incorrectly classified as positive; True Negative (TN), negative samples are correctly classified as negative; False Negative (FN), positive samples are incorrectly classified as negative. We calculate the following five indicators: True Positive Rate (TPR), $TPR = \frac{TP}{TP+FN}$; False Positive Rate (FPR), $FPR = \frac{FP}{TP+FP}$; True Negative Rate (TNR), $TNR = \frac{TN}{TN+FP}$; False Negative Rate (FNR), $FNR = \frac{FN}{TN+FN}$; Accuracy, $Accuracy = \frac{TP+TN}{TP+TN+FP+FN}$. Specifically, high TPR means that the deteriorated beverage is easily identified, and high TNR means that the undeteriorated beverage does not cause false warnings. The worst case is high FNR, which means that the deteriorated beverage does not cause a warning, which may impact the user's health. A high FPR means that an undeteriorated beverage may cause a warning, which may lead to the abandonment and waste of the still-drinkable beverage. A high accuracy indicates that the prediction of beverage deterioration and non-deterioration is accurate. The experimental results are shown in Figure 31. We found that the accuracies were more than 90.6%. Although 6.3–12.5% FPR might cause waste of beverages, and 0.0–8.3% FNR indicated that the system still failed to report deteriorated beverages, Microbe-Radar was effective and stable in monitoring the deterioration of various beverages.

6.2.3 *Ambient light Interference*

We utilized glass containers to observe the quality assessment accuracy under four ambient light scenarios: dark, sunlight, ceiling lights, and mixed lights. The experimental results in Figure 32 show that Microbe-Radar could adapt to different types of ambient light with a mean accuracy of 94.6%.

6.2.4 *Interference from Liquor Sloshing*

We created sloshing interference when Microbe-Radar was running to observe the ability to reduce such interferences. The interference was generated by walking, dropping heavy objects, stomping, hitting the brewing vessel, and moving the brewing vessel. As shown in Figure 33, Microbe-Radar

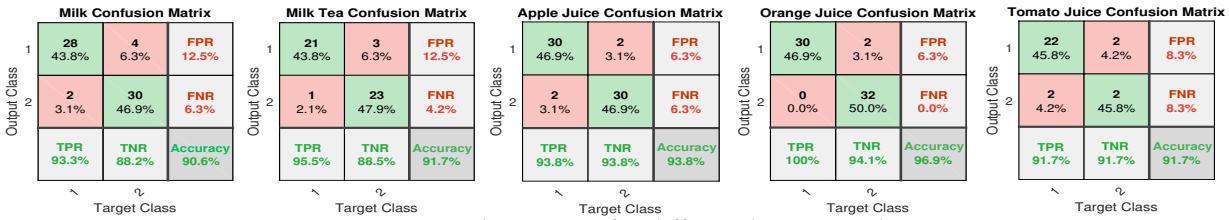

Fig. 31: TPR, FPR, FNR, TNR and Accuracy for different beverages deterioration warning.

was robust and could quickly distinguish sloshing interferences with a mean accuracy of 90.5%. The mean response time was 7.8 ms.

6.2.5 Robustness under Different Noise Levels

Microbe-Radar is used in the brewing industry, and a lot of noise will be generated in the process of mashing and boiling raw materials in the factory. Therefore, we need to check whether Microbe-Radar's monitoring ability is not disturbed by environmental noise in the noisy environment of the distillery. We conducted experiments in a distillery in Shenzhen, which covers an area of about 800 square meters. We placed the Microbe-Radar brewer at six different locations in the distillery and measured the noise level next to Microbe-Radar with the apple watch's new Noise app. The noise levels were 62 dB, 69 dB, 75 dB, 88 dB, 90 dB, and 93 dB, respectively. When the temperature was about $25°C$, we recorded the surface tension errors and absorption spectrum errors of Microbe-Radar measuring red wine for 72 hours at these different noise levels. As shown in Table 1, we found that although the noise levels differed, the measurement errors of liquid surface tension remained below 0.99 mN/m, and the measurement errors of absorption spectrum remained below 2.46%. Therefore, Microbe-Radar could operate stably in the actual distillery with a high noise level, and the errors did not increase significantly with the increase in noise level.

TABLE 1: Surface tension errors and absorption spectrum MAPEs of different noise levels and working times.

State \ Index		Surface Tension Error (mN/m)	Absorption Spectrum MAPE (%)
Noise Level	62 dB	0.89	2.31
	69 dB	0.90	2.33
	75 dB	0.92	2.35
	88 dB	0.95	2.42
	90 dB	0.94	2.41
	93 dB	0.99	2.46
Working Time	1 day	0.89	2.31
	10 days	0.90	2.35
	1 month	0.93	2.38
	3 months	0.94	2.40
	6 months	0.93	2.38

6.2.6 Stability of Long-time Measurement

Since Microbe-Radar is used in the brewing industry, whether the system can work stably for a long time cannot be ignored. We recorded the surface tension errors and absorption spectrum errors of four liquors measured by Microbe-Radar over 6 months. We kept Microbe-Radar working continuously and recorded the measurement surface tension errors and absorption spectrum errors on the first day, the tenth day, the first month, the third month, and the sixth month, respectively. As shown in Table 1, we found that liquid surface tension measurement errors were kept below 0.94 mN/m, while the measurement errors of absorption spectrum are kept below 2.40%. Therefore, Microbe-Radar could maintain the ability of stable measurement with low errors within 6 months, and the errors did not increase with time, which showed that Microbe-Radar was time-tested.

6.3 Concentration Determination

6.3.1 Microorganism Composition

Different microorganisms have unique reflectance spectra. The amount of nutrients is limited in aging, creating competition between the yeast and other microorganisms. We clustered the absorption spectrum fingerprints using the K-means method, marking the proportions of yeast and *E. coli*. As shown in Figure 34, in liquor aged with *E. coli*, the MAPE in identifying the two microorganisms was only 2.33% and 1.77%. Note that because the liquid contained other interfering substances, the sum of the two microorganism contents was not 100% during the aging period.

We also wanted to see if there were sufficient advantages in monitoring microbial composition compared to the latest optical signal systems. We modified both Nutrilyzer [45] and Smart-U [17] to match our brewing vessel. Nutrilyzer [45] consisted of 16 LEDs in the ultraviolet, visible and near-infrared regions, and two piezoelectric sensors that were attached to the lid. Smart-U [17] consisted of 12 LEDs in the visible and near-infrared regions and a photodiode, which were also attached to the lid. Nutrilyzer [45] used a neural network with the top feature subset selected by correlation-based feature selection, while Smart-U [17] used Random Forest as the prediction algorithm. Microbe-Radar utilized a self-designed dimension expansion algorithm and the K-means method. As shown in Figure 35, Microbe-Radar has the lowest MAPE, indicating that Microbe-Radar's dimension expansion technology has the exceptional capability for fine-grained monitoring.

6.3.2 Alcohol Concentration

Alcohol is produced by yeast fermentation, so the number of changes in yeast can reflect the alcohol concentration. We used the yeast content results in Section 6.3.1 to calculate yeast accumulation from the beginning of aging to the moment of sampling. Then, we used the cumulative value, liquid volume, and measurement vector $\vec{L}_{Mea}(t)$ as training parameters for the K-means method to determine the alcohol concentration. As shown in Figure 36, the alcohol content identification accuracy of the four wines during the brewing process was 88.13% on average (88.54%, 85.03%, 88.25%, and 90.74%).

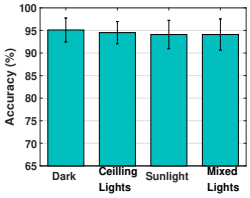

Fig. 32: Quality assessment under different ambient light noise.

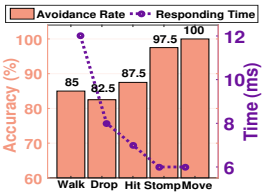

Fig. 33: Sloshing interference avoidance rate and responding time.

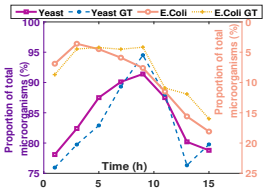

Fig. 34: Microorganisms Composition.

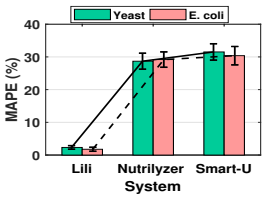

Fig. 35: Concentration determination results of different systems.

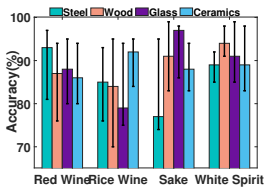

Fig. 36: Alcohol concentration measurement accuracy.

7 Related Work

In this section, we review the related literature on Microbe-Radar.

Liquid quality inspection. The conventional method of liquid quality inspection is based on the microorganisms counting method. The plate counting method [2] and ATP fluorescent microorganism detection method are the most common methods [3] applied in the liquid industry. However, they require complicated operating procedures and long-term microbial cultivation. Quality inspecting in fast and effective means is to measure the surface tension [24], [25] and absorption spectrum [18] based on the microorganism and its metabolism effect. Using the principle that the liquid's deterioration will produce different odors, the electronic nose [16] applies the odor fingerprint for inspection. However, these devices could introduce non-trivial deployment and maintenance costs. The latest working pH meter [14] uses the acid-base change of the liquid to identify whether it has deteriorated. However, its resolution is coarse-grained.

Liquid identification. There are many research achievements on liquid identification. Surface tension [26]–[28], absorption spectrum [29]–[31] and viscosity [46]–[48] are critical properties using for the fine-grained liquid components identification. They can be used to identify pollutants [49], determine blood cholesterol levels [50] and distinguish kidney diseases [22]. The latest research, Nutrilyzer [45] and Smart-U [17], apply the absorption spectrum and the photoacoustic effect to realize liquid identification. Al-light [51] proposes a smart ice cube device equipped with near-infrared and visible LEDs, which can estimate the alcohol concentration level. However, they are all limited by the narrowband spectrum of LEDs, making it challenging to identify fine-grained liquid components, such as microorganisms changes. Liquids can also affect electromagnetic signals. TagScan [20] and RFIQ [52] pay attention to the RFID signal to determine the liquid composition. LiquID [21] uses two independent ultra-wideband (UWB) units to judge the liquid by its dielectric constant. Mm-Humidity [53] uses millimeter waves to measure the liquid content in the air. The special devices or containers they use are still expensive. As a universal device, mobile phones can also identify liquids and achieve fine-grained measurements, such as surface tension [32], [33]. The latest technology is Vi-Liquid [22] and [23], which uses mobile phones to identify liquids through fine-grained viscosity differences. However, these solutions are not practical to apply to the brewing industry because they need high energy consumption and computation costs that lead to rugged use in long-term monitoring.

Light perception. As electromagnetic waves, optical signals are the common signal for perception. The object's absorption spectrum's uniqueness can be used for quality assessment [54] and food analysis [55] in the food industry. Light transmission in different media will suffer the loss of perspective and scattering, and the measurement [56] of blood oxygen concentration uses this principle. The devices which generate unique light signals can be used to achieve precise indoor localization [57], [58]. Scattered light can also be used as a sensing signal, such as sensing gestures [59]. Lili [19] is the latest technology using the light signal for alcohol and liquor production quality monitoring.

8 Conclusion and Future Work

This article presents a beverage quality monitor Microbe-Radar, the first real-time microbial contamination detection using ubiquitous sensing. A Characteristic Offset Degree Measurement model is proposed to guide the photodiode to robustly and accurately calculate the surface tension under the low signal-to-noise ratio condition. Besides, the Dimension Expansion of the Coarse-grained Absorption Spectrum model is also presented to solve the subtle changes in substances that monochromatic LEDs cannot detect. The surface tension and absorption spectrum measurement error can reach 0.89 mN/m and 2.4% (MAPE). Through the measured value, 97.5% of the hazardous-health liquors can be identified. Microbe-Radar can also predict beverage deterioration of five beverages (milk, apple juice, etc.) with an accuracy of more than 90.6%. When aging wine, it can also identify the proportion of microorganisms and alcohol concentration. However, as a proof-of-concept prototype for liquor quality measurement, Microbe-Radar still has some limitations to be addressed in our future work:

Liquid types: We aim to transition towards more feasible liquid quality monitoring situations, such as yogurt brewing and pickle pickling. The challenge of accurately assessing the dissolution of various liquids is a substantial predicament that necessitates prompt attention.

Types of containers: Numerous instances exist of expanded application situations for monitoring liquid quality. Notwithstanding, using dissimilar containers like cans and cartons presents an issue in transferring solutions for widespread tools across such varied containers. Also, adaptable device modifications, as well as size alterations, will be necessary. Looking into the future, these concerns will be deliberated upon in greater depth.

ACKNOWLEDGMENTS

This research was supported in part by the Guangdong Provincial Key Lab of Integrated Communication, Sensing and Computation for Ubiquitous Internet of Things, the China NSFC Grant (U2001207, 61872248), Guangdong NSF 2017A030312008, Shenzhen Science and Technology Foundation (No. ZDSYS20190902092853047, R2020A045), the Project of DEGP (No.2019KCXTD005), the Guangdong "Pearl River Talent Recruitment Program" under the Grant 2019ZT08X603, Guangdong Science and Technology Foundation (2019B111103001, 2019B020209001), the China NSFC 61872246, Guangdong Special Support Program. Lu Wang is the corresponding author.

REFERENCES

[1] I. O. o. V. Organization, *International code of oenological practices 2020*. International Organisation of Vine and Wine (OIV), 2020. [Online]. Available: http://www.oiv.int/public/medias/7213/oiv-international-code-of-oenological-practices-2020-en.pdf

[2] B. Herigstad, M. Hamilton, and J. Heersink, "How to optimize the drop plate method for enumerating bacteria," *Journal of microbiological methods*, vol. 44, no. 2, pp. 121–129, 2001.

[3] K. Sakamoto, A. Margolles, H. W. Van Veen, and W. N. Konings, "Hop resistance in the beer spoilage bacterium Lactobacillus brevis is mediated by the ATP-binding cassette multidrug transporter HorA," *Journal of bacteriology*, vol. 183, no. 18, pp. 5371–5375, 2001.

[4] P. R. Grbin and P. A. HENSCHKE, "Mousy off-flavour production in grape juice and wine by dekkera and brettanomyces yeasts," *Australian Journal of Grape and Wine Research*, vol. 6, no. 3, pp. 255–262, 2000.

[5] H. Piao, E. Hawley, S. Kopf, R. DeScenzo, S. Sealock, T. Henick-Kling, and M. Hess, "Insights into the bacterial community and its temporal succession during the fermentation of wine grapes," *Frontiers in microbiology*, vol. 6, p. 809, 2015.

[6] F. Käferstein and M. Abdussalam, "Food safety in the 21st century." *Bulletin of the World Health Organization*, vol. 77, no. 4, p. 347, 1999.

[7] P. S. Mead, L. Slutsker, V. Dietz, L. F. McCaig, J. S. Bresee, C. Shapiro, P. M. Griffin, and R. V. Tauxe, "Food-related illness and death in the United States." *Emerging infectious diseases*, vol. 5, no. 5, p. 607, 1999.

[8] S. Hoffmann and E. Scallan, "Epidemiology, cost, and risk analysis of foodborne disease," in *Foodborne Diseases*. Elsevier, 2017, pp. 31–63.

[9] V. Fusco, D. Chieffi, F. Fanelli, A. F. Logrieco, G.-S. Cho, J. Kabisch, C. Böhnlein, and C. M. A. P. Franz, "Microbial quality and safety of milk and milk products in the 21st century," *Comprehensive Reviews in Food Science and Food Safety*, vol. 19, no. 4, pp. 2013–2049, 2020.

[10] Z. Gizaw, "Public health risks related to food safety issues in the food market: a systematic literature review," *Environmental health and preventive medicine*, vol. 24, no. 1, pp. 1–21, 2019.

[11] Z. Xu, Y. Luo, Y. Mao, R. Peng, J. Chen, T. Soteyome, C. Bai, L. Chen, Y. Liang, J. Su, and Others, "Spoilage lactic acid bacteria in the brewing industry," *Journal of microbiology and biotechnology*, vol. 30, no. 7, pp. 955–961, 2020.

[12] J. H. J. H. in't Veld, "Microbial and biochemical spoilage of foods: an overview," *International journal of food microbiology*, vol. 33, no. 1, pp. 1–18, 1996.

[13] W. H. Organization and Others, *WHO estimates of the global burden of foodborne diseases: foodborne disease burden epidemiology reference group 2007-2015*. World Health Organization, 2015.

[14] P. M. Shaibani, H. Etayash, K. Jiang, A. Sohrabi, M. Hassanpourfard, S. Naicker, M. Sadrzadeh, and T. Thundat, "Portable nanofiber-light addressable potentiometric sensor for rapid Escherichia coli detection in orange juice," *ACS sensors*, vol. 3, no. 4, pp. 815–822, 2018.

[15] A. F. Cunha, A. D. Lage, M. M. e Araújo, C. F. Abreu, A. R. Tassinari, M. A. Ferraz, K. Davenport, and M. Cerqueira, "ATP-Bioluminescence as a method to evaluated microbiological quality of UHT milk," *Arquivo Brasileiro de Medicina Veterinária e Zootecnia*, vol. 66, no. 6, pp. 1909–1916, 2014.

[16] M. L. Rodr\'\iguez-Méndez, J. A. De Saja, R. González-Antón, C. Garc\'\ia-Hernández, C. Medina-Plaza, C. Garc\'\ia-Cabezón, and F. Mart\'\in-Pedrosa, "Electronic noses and tongues in wine industry," *Frontiers in bioengineering and biotechnology*, vol. 4, p. 81, 2016.

[17] Q. Huang, Z. Yang, and Q. Zhang, "Smart-U: Smart Utensils Know what You Eat," in *Proceedings - IEEE INFOCOM*, vol. 2018-April. IEEE, 2018, pp. 1439–1447.

[18] H. M. Al-Qadiri, M. Lin, M. A. Al-Holy, A. G. Cavinato, and B. A. Rasco, "Monitoring quality loss of pasteurized skim milk using visible and short wavelength near-infrared spectroscopy and multivariate analysis," *Journal of dairy science*, vol. 91, no. 3, pp. 950–958, 2008.

[19] Y. Huang, K. Chen, L. Wang, Y. Dong, Q. Huang, and K. Wu, "Lili: liquor quality monitoring based on light signals," in *Proceedings of the 27th Annual International Conference on Mobile Computing and Networking*, 2021, pp. 256–268.

[20] J. Wang, J. Xiong, X. Chen, H. Jiang, R. K. Balan, and D. Fang, "TagScan: Simultaneous target imaging and material identification with commodity RFID devices," in *Proceedings of the Annual International Conference on Mobile Computing and Networking, MOBICOM*, vol. Part F131210, 2017, pp. 288–300.

[21] A. Dhekne, M. Gowda, Y. Zhao, H. Hassanieh, and R. R. Choudhury, "LiquID: A wireless liquid identifier," in *MobiSys 2018 - Proceedings of the 16th ACM International Conference on Mobile Systems, Applications, and Services*, 2018, pp. 442–454.

[22] Y. Huang, K. Chen, Y. Huang, L. Wang, and K. Wu, "Vi-liquid: unknown liquid identification with your smartphone vibration." in *MobiCom*, 2021, pp. 174–187.

[23] ——, "A portable and convenient system for unknown liquid identification with smartphone vibration," *IEEE Transactions on Mobile Computing*, 2021.

[24] D. K. Ayhan, A. Temiz, F. A. Sana, and M. Gümü\csderelio\uglu, "Surface properties and exopolysaccharide production of surface-associated microorganisms isolated from a dairy plant," *Annals of Microbiology*, vol. 69, no. 9, pp. 895–907, 2019.

[25] Z. J. Mai, F. Lin, and J. M. Fan, "Research of Monitoring Deterioration of Milk by Using Surface Tension Coefficient and Viscosity," in *Advanced Materials Research*, vol. 455. Trans Tech Publ, 2012, pp. 467–470.

[26] V. B. Fainerman, R. Miller, and P. Joos, "The measurement of dynamic surface tension by the maximum bubble pressure method," *Colloid and Polymer Science*, vol. 272, no. 6, pp. 731–739, 1994.

[27] W. D. Harkins and F. E. Brown, "The determination of surface tension (free surface energy), and the weight of falling drops: The surface tension of water and benzene by the capillary height method." *Journal of the American Chemical Society*, vol. 41, no. 4, pp. 499–524, 1919.

[28] C. E. Stauffer, "The measurement of surface tension by the pendant drop technique," *The journal of physical chemistry*, vol. 69, no. 6, pp. 1933–1938, 1965.

[29] E. J. Hart and J. W. Boag, "Absorption spectrum of the hydrated electron in water and in aqueous solutions," *Journal of the American Chemical Society*, vol. 84, no. 21, pp. 4090–4095, 1962.

[30] L. N. M. Duyens, "The flattering of the absorption spectrum of suspensions, as compared to that of solutions," *Biochimica et biophysica acta*, vol. 19, pp. 1–12, 1956.

[31] R. M. Pope and E. S. Fry, "Absorption spectrum (380–700 nm) of pure water. II. Integrating cavity measurements," *Applied optics*, vol. 36, no. 33, pp. 8710–8723, 1997.

[32] N.-A. Goy, Z. Denis, M. Lavaud, A. Grolleau, N. Dufour, A. Deblais, and U. Delabre, "Surface tension measurements with a smartphone," *The Physics Teacher*, vol. 55, no. 8, pp. 498–499, 2017.

[33] S. Yue and D. Katabi, "Liquid testing with your smartphone," in *MobiSys 2019 - Proceedings of the 17th Annual International Conference on Mobile Systems, Applications, and Services*, 2019, pp. 275–286.

[34] T. K. Barik, P. R. Chaudhuri, A. Roy, and S. Kar, "Probing liquid surface waves, liquid properties and liquid films with light diffraction," *Measurement Science and Technology*, vol. 17, no. 6, p. 1553, 2006.

[35] M. Wei, S. Huang, J. Wang, H. Li, H. Yang, and S. Wang, "The study of liquid surface waves with a smartphone camera and an image recognition algorithm," *European Journal of Physics*, vol. 36, no. 6, p. 65026, 2015.

[36] A. J. T. Van Loon, *Analytical atomic absorption spectroscopy: selected methods*. Elsevier, 2012.

[37] C. Little, D. Lock, J. Barnes, and R. Mitchell, "Microbiological quality of food in relation to hazard analysis systems and food hygiene training in uk catering and retail premises." *Communicable disease and public health*, vol. 6, no. 3, pp. 250–258, 2003.

[38] H. P. A. o. U. Organization, *Guidelines for Assessing the Microbiological Safety of Ready-to-Eat Foods Placed on the Market*. Health Protection Agency of UK, 2009. [Online]. Available: https://assets.publishing.service.gov.uk/government/uploads/system/uploads/attachment_data/file/363146/Guidelines_for_assessing_the_microbiological_safety_of_ready-to-eat_foods_on_the_market.pdf

[39] F. Edition, "Guidelines for drinking-water quality," *WHO chronicle*, vol. 38, no. 4, pp. 104–108, 2011.

[40] J. O. Lundberg, M. T. Gladwin, A. Ahluwalia, N. Benjamin, N. S. Bryan, A. Butler, P. Cabrales, A. Fago, M. Feelisch, P. C. Ford *et al.*, "Nitrate and nitrite in biology, nutrition and therapeutics," *Nature chemical biology*, vol. 5, no. 12, pp. 865–869, 2009.

[41] S. Clegg, F. Yu, L. Griffiths, and J. A. Cole, "The roles of the polytopic membrane proteins nark, naru and nirc in escherichia coli k-12: two nitrate and three nitrite transporters," *Molecular microbiology*, vol. 44, no. 1, pp. 143–155, 2002.

[42] H. Muhamadali, A. Subaihi, M. Mohammadtaheri, Y. Xu, D. I. Ellis, R. Ramanathan, V. Bansal, and R. Goodacre, "Rapid, accurate, and comparative differentiation of clinically and industrially relevant microorganisms via multiple vibrational spectroscopic fingerprinting," *Analyst*, vol. 141, no. 17, pp. 5127–5136, 2016.

[43] K. Wang, H. Pu, and D.-W. Sun, "Emerging spectroscopic and spectral imaging techniques for the rapid detection of microorganisms: An overview," *Comprehensive reviews in food science and food safety*, vol. 17, no. 2, pp. 256–273, 2018.

[44] Y. Ohno, "Spectral design considerations for white LED color rendering," *Optical Engineering*, vol. 44, no. 11, p. 111302, 2005.

[45] T. Rahman, A. T. Adams, P. Schein, A. Jain, D. Erickson, and T. Choudhury, "Nutrilyzer: A mobile system for characterizing liquid food with photoacoustic effect," in *Proceedings of the 14th ACM Conference on Embedded Networked Sensor Systems, SenSys 2016*, 2016, pp. 123–136.

[46] J. de Vicente, M. T. López-López, J. D. Durán, and F. González-Caballero, "Shear flow behavior of confined magnetorheological fluids at low magnetic field strengths," *Rheologica Acta*, vol. 44, no. 1, pp. 94–103, 2004.

[47] C. Blom and J. Mellema, "Torsion pendula with electromagnetic drive and detection system for measuring the complex shear modulus of liquids in the frequency range 80-2500 Hz," *Rheologica Acta*, vol. 23, no. 1, pp. 98–105, 1984.

[48] M. Gottlieb, "Zero-shear-rate viscosity measurements for polymer solutions by falling ball viscometry," *Journal of Non-Newtonian Fluid Mechanics*, vol. 6, no. 2, pp. 97–109, 1979.

[49] I. N. Aribudiman, "Seepage in soil from the difference of water viscosity using Geo-studio SEEP/W program," *International research journal of engineering, IT & scientific research*, vol. 5, no. 1, pp. 15–26, 2019.

[50] C. Tripolino, C. Irace, C. Carallo, F. B. Scavelli, and A. Gnasso, "Body fat and blood rheology: Evaluation of the association between different adiposity indices and blood viscosity," *Clinical Hemorheology and Microcirculation*, vol. 65, no. 3, pp. 241–248, 2017.

[51] H. Matsui, T. Hashizume, and K. Yatani, "Al-light: An Alcohol-Sensing Smart Ice Cube," *Proceedings of the ACM on Interactive, Mobile, Wearable and Ubiquitous Technologies*, vol. 2, no. 3, pp. 1–20, 2018.

[52] U. Ha, Y. Ma, Z. Zhong, T. M. Hsu, and F. Adib, "Learning food quality and safety from wireless stickers," in *HotNets 2018 - Proceedings of the 2018 ACM Workshop on Hot Topics in Networks*, 2018, pp. 106–112.

[53] Q. Dai, Y. Huang, L. Wang, R. Ruby, and K. Wu, "mm- humidity: Fine-grained humidity sensing with millimeter wave signals," in *2018 IEEE 24th International Conference on Parallel and Distributed Systems (ICPADS)*, 2018, pp. 204–211.

[54] N. Prieto, R. Roehe, P. Lav\'\in, G. Batten, and S. Andrés, "Application of near infrared reflectance spectroscopy to predict meat and meat products quality: A review," *Meat science*, vol. 83, no. 2, pp. 175–186, 2009.

[55] Y. Ozaki, W. F. McClure, and A. A. Christy, *Near-infrared spectroscopy in food science and technology*. John Wiley & Sons, 2006.

[56] F. Gao, Q. Peng, X. Feng, B. Gao, and Y. Zheng, "Single-wavelength blood oxygen saturation sensing with combined optical absorption and scattering," *IEEE Sensors Journal*, vol. 16, no. 7, pp. 1943–1948, 2015.

[57] C. Zhang and X. Zhang, "Pulsar: Towards ubiquitous visible light localization," in *Proceedings of the 23rd Annual International Conference on Mobile Computing and Networking*, 2017, pp. 208–221.

[58] ——, "LiTell: Robust indoor localization using unmodified light fixtures," in *Proceedings of the 22nd Annual International Conference on Mobile Computing and Networking*, 2016, pp. 230–242.

[59] R. H. Venkatnarayan and M. Shahzad, "Gesture recognition using ambient light," *Proceedings of the ACM on Interactive, Mobile, Wearable and Ubiquitous Technologies*, vol. 2, no. 1, pp. 1–28, 2018.

Yongzhi Huang is currently the Ph.D. in the HongKong University Science and Technology (Guangzhou). He received his B.S. and M.S. from Shenzhen University. His research interests include smart sensing, mobile computing, and the Internet of Things (IoT). He has published papers in primary conferences and journals, such as ACM MobiCom, Ubicomp, IEEE TMC, etc. He is the inventor of 12 Chinese pending patents (2 are issued).

Kaixin Chen is studying for a master's degree at the College of Computer Science and Software Engineering, Shenzhen University. He published papers in primary conferences, such as ACM MobiCom, etc. His research interest lies in mobile computing and the Internet of Things (IoT).

Jiayi Zhao is studying for a master's degree at the College of Computer Science and Software Engineering, Shenzhen University. Her research interest lies in mobile computing and Internet of Things (IoT).

Lu Wang is currently an assistant professor in the College of Computer Science and Software Engineering, Shenzhen University, China. Her research interests focus on wireless communications and mobile computing.

Kaishun Wu received his Ph.D. degree in computer science and engineering from HKUST in 2011. After that, he worked as a research assistant professor at HKUST. In 2013, he joined SZU as a distinguished professor. He has co-authored 2 books and published over 100 high-quality research papers in international leading journals and primer conferences, like IEEE TMC, IEEE TPDS, ACM MobiCom, IEEE INFOCOM. He is the inventor of 6 US and over 90 Chinese pending patents. He received 2012 Hong Kong Young Scientist Award, the 2014 Hong Kong ICT Awards: Best Innovation and 2014 IEEE ComSoc Asia-Pacific Outstanding Young Researcher Award. He is an IET Fellow.